Journal of Materials Science: Materials in Engineering

ORIGINAL PAPER

Open Access

Bismuth oxyiodides: photocatalytic performance, by-products, and degradation pathways

Andrea Martinez-Topete[1,2], Eva Jimenez-Relinque[1], Frederic Dappozze[3], Sofia Salli[4], Aziz Genç[5], Thomas Slater[5], Chantal Guillard[3], Andrea Folli[6] and Marta Castellote[1*]

Abstract

The increasing global demand for environmental remediation strategies has led to significant interest in the development of efficient photocatalysts. Semiconductor photocatalysts, such as titanium dioxide (TiO_2 P25), have been extensively studied for addressing challenges such as water purification and air decontamination. However, TiO_2 P25's wide band gap restricts its efficacy under visible light, which limits its practical use in real-life applications. Bismuth oxyiodides have emerged as highly promising alternatives due to their narrow band gaps and visible-light responsiveness. In this study, BiOI, Bi_5O_7I, and BiOI/Bi_5O_7I have been synthesized by pH-dependent co-precipitation and hydrothermal methods and evaluated their photocatalytic performance for phenol degradation and nitrogen oxides (NO_x) oxidation. Under visible light irradiation, BiOI-co pH 10 and BiOI/Bi_5O_7I-co pH 12 demonstrated promising phenol degradation rates (≈51%) compared to the TiO_2 P25 benchmark (≈ 11%). In terms of mineralization efficiency, as measured by the total organic carbon (TOC)/phenol ratio (0.6–0.7), Bi_5O_7I-UV, BiOI/Bi_5O_7I-VIS, and TiO_2 P25-UV showed similar capabilities. Only under UV light irradiation did TiO_2 P25 (phenol removal≈100%; NO removal≈86%) surpass the bismuth oxyiodides. Despite showing minimal production of aromatic by-products (e.g., hydroquinone, benzoquinone, and catechol) during phenol degradation, the bismuth oxyiodides exhibited higher NO_2 production compared to TiO_2 P25 during NO_x oxidation. One possible explanation for this phenomenon may be attributed to different ROS-mediated mechanisms present in TiO_2 P25 and bismuth oxyiodide compounds. However, the possibility of significant adsorption of intermediates in solution onto bismuth oxyiodide materials cannot be neglected. Quencher experiments, electron paramagnetic resonance (EPR), and terephthalic acid-fluorescence probe method revealed that hydroxyl radicals (HO·) are not the major oxidant specie in in bismuth oxyiodide-mediated photocatalysis. Using evidence from EPR spectroscopy, a photodegradation pathway, involving singlet oxygen ($^1O_2$), was proposed. These findings provide valuable insights into the photocatalytic behavior of bismuth oxyiodides and highlights the importance of understanding the mechanisms to optimize their use for environmental applications.

Keywords Bismuth oxyiodides, Photocatalysis, NO_x, Phenol, By-products, ROS-mediated mechanism

*Correspondence:
Marta Castellote
martaca@ietcc.csic.es
Full list of author information is available at the end of the article

Introduction

The interest in semiconductor photocatalysts has grown due to its wide range of potential applications in solar energy conversion (Yang et al. 2018; Kaleem Ahmad and Ahuja 2020) and environmental remediation (Yang et al. 2018; Kaleem Ahmad and Ahuja 2020; Michael et al. 1995; J.a.Y. Zhao, X.D. 2003; J.n.B. Sixto Malato, Alfonso Vidal, Christoph Richter 2002; Herrmann et al. 1993). Titanium dioxide (TiO_2) nanoparticles are the most widely used semiconductor photocatalyst (Fujishima et al. 2000; Schneider et al. 2014). However, its efficiency under solar irradiation for real-life applications is limited by its wide band gap (3.0–3.2 eV) (Alcaraz et al. 2020; Jimenez-Relinque et al. 2017). This means that only $3-5\%$ of solar light throughout the whole year at latitudes below 35° (tropical and subtropical region) can be utilized by the conventional TiO_2-based photocatalyts. As latitude increases, this value may drop lower than $3-5\%$ (Folli et al. 2014). Furthermore, TiO_2 nanoparticles could cause adverse health effects if inhaled (cell damage, genotoxicity, inflammation, and immune response) as well as environmental contamination (Skocaj et al. 2011; Nevshupa et al. 2020; Jimenez-Relinque et al. 2020). As a result, the development of novel micro-sized solar-light-driven photocatalysts and the investigation of their photocatalysis activities are essential.

Bismuth oxyiodide, BiOI, is among the most promising photocatalysts due to its narrow band gap (≈1.7–1.9 eV) making it a possible visible light-responding photocatalyst. The morphology of BiOI structures is drastically influenced by the synthesis method. Various morphologies of BiOI, including nanosheets (Hu et al. 2014; Ye et al. 2016), hierarchical nanostructures (Long et al. 2016; Shi et al. 2012), and microspheres (Xiao and Zhang 2010; Mera et al. 2017; Nava-Núñez et al. 2020), have been successfully obtained. It has also been observed that morphology influences photocatalytic efficacy. For instance, Hao et al. reported that the photocatalytic activity of BiOI microspheres was more than double than that obtained for nanosheets in the degradation of tetracycline hydrochloride under visible light irradiation (Hao et al. 2012). Martinez-Topete et al. observed similar trend for NO_x oxidation (Martinez-Topete et al. 2025). Xiao et al. and Hu et al. reported similar results for phenol degradation and As(III) oxidation, respectively (Hu et al. 2014; Xiao and Zhang 2010). However, at the same time, the insufficient redox ability of BiOI can be dissatisfactory because of the narrow band gap and unmatched energy band position (Dai and Zhao 2016; Cai et al. 2019; Ahmad et al. 2022; Zuarez-Chamba et al. 2023; Geng et al. 2024).

Recently, Bi-rich bismuth oxyiodides, $Bi_xO_yI_z$ ($Bi_7O_9I_3$, $Bi_4O_5I_2$, and Bi_5O_7I) have been proposed as potential alternative photocatalysts. These materials can effectively be prepared by adjusting synthesis parameters such as solvent, temperature, or pH (Martinez-Topete et al. 2025; Geng et al. 2024; Yu et al. 2015; Jimenez-Relinque et al. 2024; Wei et al. 2019; Wu et al. 2018; Di et al. 2017; Xiao et al. 2014). Increasing the amount of Bi in oxyiodides leads to a more cathodic conduction band (CB) edge, a more anodic valence (VB) edge, or both, compared to BiOI. This can improve the thermodynamics of the reduction and oxidation reactions driven by the light-irradiated bismuth oxyiodides following electron–hole pairs formation (Xiong et al. 2020; Jin et al. 2017). For instance, $Bi_4O_5I_2$ possesses a wider band gap than BiOI (≈2.2–2.7 eV) and showed superior photocatalytic (almost twice) and mineralization efficiencies compared with BiOI under visible-light irradiation (Zuarez-Chamba et al. 2023; Xiao et al. 2014; Zhang et al. 2022). $Bi_7O_9I_3$ has been reported as a solar-light-driven photocatalyst (E_g≈2.2–2.9 eV) capable of degrading organic pollutants (Xiao et al. 2012; Ma et al. 2022; Matiur et al. 2021; Tuba-Guaman et al. 2022; Liu et al. 2023). Bi_5O_7I has a wide band gap of 2.75 eV with a remarkable photocatalytic nitrogen fixation performance (Lan et al. 2020). Although in literature it is generally assumed that increasing the Bi-to-I ratio is an innovative strategy to enhance photocatalytic efficiency (Xiong et al. 2020), this modulation can produce an implicit reduction in visible light absorption (Geng et al. 2024; Lan et al. 2020), non-favorable band potentials for the target reactions (Jimenez-Relinque et al. 2024), increase in e^--h^+ recombination (Arumugam and Choi 2020), or even the generation of unwanted by-products (Wang et al. 2021; Kynadi and Suchithra 2017).

Since reactive oxygen species (ROS) are primary intermediates of photocatalytic reactions, their identification is important in terms of understanding the photodegradation mechanisms. Four major ROS are recognized, comprising superoxide anion radical ($O_2{\cdot}^-$), hydrogen peroxide (H_2O_2), singlet oxygen ($^1O_2$), and hydroxyl radical (HO·) (Nosaka and Nosaka 2017). For bismuth oxyiodides photocatalysts, divergent conclusions are remarked for the major oxidants involved in the photocatalytic degradation reactions. Liu et al. reported that $O_2{\cdot}^-$ and h^+ species are primarily involved in the photodegradation of organic pollutants in solution by $Bi_7O_9I_3$ (Liu et al. 2023). In contrast, Wei et al. state that the oxidation of organics by $Bi_7O_9I_3$ system is preferentially through a non-radical pathway mediated by the iodine vacancies, verifying no $^1O_2$ generation (Wei et al. 2019). For $Bi_4O_5I_2$, it was seen that h^+, $O_2{\cdot}^-$, and e^- were the species involved (Xiao et al. 2014; Zhang et al. 2022). Formation of HO· and $O_2{\cdot}^-$ was detected for bare rod-like Bi_5O_7I and flower-like Bi_5O_7I and BiOI (Wang et al. 2017a; Chen et al. 2018). Since there is a wide variety of results regarding the ROS generated by bismuth oxyiodides, further studies should

be carried out to fully understand the mechanism and involved active species. Also, it should be kept in mind that slight differences in synthesis routes can lead to catalysts with significantly different photocatalytic properties, even if they have the same crystalline phase.

In this work, BiOI, Bi_5O_7I, and their combinations with different morphologies were synthesized using a sustainable, room temperature, and pH-dependent co-precipitation method. Their photocatalytic performance under both UV and visible light was assessed for aqueous phenol degradation and nitrogen oxides (NO_x) oxidation, providing a comprehensive understanding of the photocatalytic behavior under various environmental conditions. The study also highlights the importance of analyzing reaction intermediates and byproducts, which are often overlooked in the literature but are critical for evaluating the environmental impact of photocatalytic processes. The results were compared to those obtained using TiO_2 P25 as a benchmark, in terms of both photocatalytic efficiency and the formation of potentially harmful intermediates. Additionally, we provide evidence that hydroxyl radicals (HO·) may not be the primary reactive species in bismuth oxyiodide photocatalytic systems, even for the Bi_5O_7I crystal structure, whose valence band potential theoretically supports HO· formation from water oxidation. Instead, a plausible mechanism involving singlet oxygen ($^1O_2$) as the key reactive oxygen species is proposed — this mechanism, to the best of our knowledge, has not been previously reported for these materials. These findings not only underscore the potential of bismuth oxyiodides as efficient photocatalysts but also emphasize the need to carefully consider reaction intermediates, mechanisms, and reaction conditions to optimize their practical applications for environmental remediation.

Experimental procedure

Synthesis of bismuth oxyiodides

Bismuth oxyiodides were synthesized via coprecipitation and hydrothermal procedures using bismuth (III) nitrate pentahydrate ($Bi(NO_3)_3{\cdot}5H_2O, \geq 98\%$, Sigma-Aldrich) and potassium iodide (KI, Scharlau) as starting materials. The co-precipitation synthetic processes of BiOI, BiOI/Bi_5O_7I, and Bi_5O_7I crystals were prepared with a stoichiometric Bi/I molar ratio of 1:1, employing different pH conditions (1, 10, 12, and 13). The sample Bi_5O_7I was also synthesized via the hydrothermal method at same pH condition (13) to confirm that there were no significant differences in structure or photocatalytic performance compared to the sustainable co-precipitation method proposed. Each synthesis was performed at least in triplicate to verify the reproducibility of the preparation procedure. This has been confirmed through X-ray diffraction (XRD) (Fig. S1).

In the co-precipitation synthesis procedure, KI (0.02 mol) was dissolved in 150 mL of deionized H_2O. $Bi(NO_3)_3{\cdot}5H_2O$ (0.02 mol) was slowly added to the above solution. The pH of the mixture was adjusted to 10, 12, and 13 using a NaOH 2 M solution, and the mixture was vigorously stirred for 24 h at room temperature. In the hydrothermal synthesis, equal amount of moles of both starting materials was dissolved in 50 mL of NaOH 1 M and stirred for 20 min. The resulting suspension was transferred to a 100 mL Teflon-lined stainless steel autoclave and heated for 24 h at 160 °C. At last, the resulting solid products were collected by filtration, washed several times with deionized water (1.5 L), and dried in an air oven at 65 °C for 24 h.

The synthesized materials were systematically labeled as follows: *X*–*y*, where *X* denotes the crystal phase of the product and *y* represents the synthesis method, either coprecipitation (co) or hydrothermal (hy). The pH conditions were also specified.

Characterization

The phase composition and structure of the as-prepared powders were examined by X-ray diffraction (XRD) spectroscopy using a Bruker D8 Advance diffractometer with Cu-Ka radiation (40 kV, 30 mA). The morphologies were determined using a field emission scanning electron microscope (FESEM) equipped with an energy-dispersive X-ray spectroscope (SEM–EDS; Hitachi S-4800). The aforementioned FESEM is provided with a Bruker Nano XFlash Detector 5030 for energy-dispersive X-ray (EDX) analysis. Transmission electron microscopy (TEM) analyses were performed on a JEOL JEM-2100 operating at 200 kV. Fourier transform infrared spectroscopy (FTIR) spectra were obtained using a Thermo Scientific Nicolet 6700 spectrometer. Nitrogen adsorption isotherms were recorded with an automated system (Micromeritics ASAP 2010) for later determination of Brunauer–Emmett–Teller (BET) specific surface areas (S_{BET}). The particle size distribution has been analyzed with a Mastersizer 3000 (MAL1203757). A UV-2600 Shimadzu spectrometer was used to record diffuse reflectance (DR) ultraviolet–visible (UV–Vis) spectra in the 200–900-nm wavelength range at room temperature. Mott-Schottky plot measurements were performed using an AutoLab potentiostat at 1000 Hz. The setup consisted on a three-electrode cell with a thin film of the photocatalyst over FTO as working electrode, a Pt wire as counter electrode, and an Ag/AgCl 3 M KCl as reference electrode. 0.2 M Na_2SO_4 (pH 7.5) was used as electrolyte. The photoluminescence (PL) spectra were measured by a Perkin-Elmer

LS-55 fluorescence spectrometer with an excitation wavelength of 315 nm.

Photocatalytic performance and identification of intermediate products

The photocatalytic performances of as-synthesized samples were evaluated by nitrogen oxide ($NO_x = NO + NO_2$) air purification and phenol degradation in aqueous solution under UV and visible light irradiation.

NO_x oxidation measurements were performed in a continuous flow reactor based on the requirements of ISO standard 22,197–1:2007. For this test, thin films (6.5 cm^2) containing 10 ± 2 mg of sample were prepared. The performance of each sample was tested under UV (Philips BLB 15W) and visible light (Philips Master TL-D 15W, with filter up to 425 nm). The spectra of the lamps used are depicted in Fig. S2. The irradiance was measured with a DeltaOHM HD 2102.1 photo/radiometer, obtaining 10 ± 1 and 15 ± 1 W/m^2, respectively. As inlet gas, NO diluted in air with a concentration of 500 ± 50 ppb and flow rate controlled at 1 L/min was used. After reaching the adsorption–desorption equilibrium, the sample was irradiated for 30 min. The NO_x concentration in the gas was monitored using a AC32M Environmental S.A. chemiluminescence analyzer. Efficiencies for NO and NO_x removal, NO_2 formed, and nitrate selectivity ($\frac{NO_{x\,removal}}{NO_{removal}} \cdot 100$) (Bloh et al. 2014) were determined. The results were extrapolated to ISO standard 22,197–1:2007 nominal area (49.25 cm^2) and irradiance (10 W/m^2) requirements.

Phenol degradation in water solution tests were performed in a 100 mL glass photoreactor, using a 0.2 mM phenol aqueous solution with a photocatalyst concentration of 1 g/L. The experimental procedure was as follows: 30 mg of catalyst powder was dispersed into 30 mL of the contaminant solution, which was then stirred for 30 min in the dark to ensure the establishment of adsorption–desorption equilibrium. Following that, the contaminant solution containing photocatalyst was irradiated for 180 min. The performance of each sample was tested under UV (Philips PLL UV-A 18W) centered at 370 nm and visible light (white LED) (Fig. S2), with photon fluxes measured with CCD AvaSpec-2048 of 253 ± 1 and 3372 ± 10 photons/s/m^2, respectively, and irradiances measured with a DeltaOHM HD 2102.1 photo/radiometer of 20 ± 2 and 800 ± 80 W/m^2, respectively. During this period, approximately 0.5 mL of the suspension was taken out every 30 min. HPLC analyses were performed using a Shimadzu SPD-M40 system with a diode array detector to follow the total conversion of phenol and the yield of possibly formed aromatic intermediates such as benzoquinones, hydroquinone, and catechol (Turki et al. 2015). A 15 cm × 4.6 mm × 2.7-µm Ascentis® Express 90 AQ-C18 reverse-phase column (Supelco® Merck) was used. Mobile phase consisted in 95% of acidified water (with 0.1% w/w of formic acid) and 5% of methanol.

Total organic carbon (TOC) analyses of the samples with the best performance were done using a TOC-L Shimadzu to assess the degree of mineralization achieved after 180 min of irradiation. A total of 20 mg of catalyst were added to 20 mL of the contaminant solution (phenol 0.2 mM) and irradiated with UV (Philips Actinic BL 15 W; $I = 20 \pm 2$ W/m^2) or visible (Philips Master TL-D 15W; $I = 76 \pm 2$ W/m^2) light.

^{1}H NMR tests were also used to validate intermediate formation during phenol photodecomposition. A total of 25 mg of catalyst were added to 5 mL of a phenol 1-mM solution in D_2O, stirred for 30 min in the dark, and then exposed to UV (Philips Actinic BL 15W; $I = 20 \pm 2$ W/m^2) and visible (Philips Master TL-D 15W; $I = 76 \pm 2$ W/m^2) light for 180 min. ^{1}H NMR (D_2O) spectra of the samples were recorded with a Bruker AV 600 MHz spectrometer equipped with a cryoprobe for sensibility gaining. Phenol degradation was monitored via UV–Vis absorption spectra (UV-2600 Shimadzu spectrometer).

Reusability tests

Reusability tests to analyze the catalysts stability were carried out with the samples that exhibited the best phenol degradation rates. For it, 20 mg of catalyst was added to 20 mL of the contaminant solution (phenol 0.2 mM). The suspension was stirred for 30 min in dark and then exposed to UV (Philips Actinic BL 15 W; $I = 20 \pm 2$ W/m^2) or visible (Philips Master TL-D 15W; $I = 76 \pm 2$ W/m^2) light for 180 min. The catalyst was removed through centrifugation and washed with water. The assay was repeated three times. The phenol degradation was monitored via UV–Vis absorption spectra at a maximum λ_{Abs} of 369 nm (UV-2600 Shimadzu spectrometer).

Reactive species experiments

To evaluate the generation of HO·, isopropyl alcohol (IPA) phenol scavenger (Liu et al. 2019; Ge et al. 2022; Bairamis and Konstantinou 2021) and terephthalic acid (TA) fluorescence (Jimenez-Relinque and Castellote 2018) experiments were carried out. The method of IPA quencher was similar to the previously reported phenol photocatalytic activity test. A scavenger-phenol 25:1 ratio was used. A total of 20 mg of catalyst were added to 20 mL of a 0.2 M phenol solution in the presence of IPA (5 mM), and the suspension was stirred for 30 min in the dark and then exposed to UV light (Philips Actinic BL 15 W; $I = 20 \pm 2$ W/m^2) for 180 min. During this period, approximately 4 mL of the suspension was taken out every 45 min, and the phenol degradation was monitored

via UV–Vis absorption spectra (UV-2600 Shimadzu spectrometer).

For the terephthalic acid (TA) fluorescence assays, 20 mg of catalyst was added to 100 mL of a 2 mM TA aqueous solution containing 2-mM NaOH, and the suspension was stirred and irradiated under UV light (Philips BLB 15 W; $I = 10 \pm 1$ W/m^2). Approximately, 4.5 mL of the suspension was taken out at the following time intervals: 2.5, 5, 10, 15, and 20 min, and centrifuged to remove the photocatalysts, and the FL intensity of the supernatant solution was measured at 425 nm ($\lambda_{exc} = 315$ nm) using a Perkin-Elmer LS-55 fluorescence spectrometer to confirm the formation of fluorescent 2-hydroxyterephthalic acid (TAOH).

For identifying the photogenerated reactive species in the photocatalytic reaction 5,5-dimethyl-1-pyrroline N-oxide (DMPO), spin-trap electron paramagnetic resonance experiments were done. For that, a water suspension of the catalyst with DMPO (30 mM) was stirred and irradiated under UV light for 5 min. EPR spectra were recorded at room temperature using a Bruker EMX micro spectrometer equipped with a Bruker ER-4123d dielectric resonator operating at X-band frequency. Spectra were recorded at 100 kHz magnetic induction modulation frequency, 0.1 mT magnetic induction modulation amplitude, 5.12 ms time constant, 10.24 ms conversion time, 10^4 receiver gain, and 2 mW microwave power. Each spectrum was recorded using 10 accumulation scans.

Results and discussion

Composition and morphology

Figure 1 shows the diffraction patterns of the bismuth oxyiodides samples synthesized at different pH via co-precipitation and hydrothermal procedures, along with the reference peaks for bismuth oxyiodides BiOI (COD 9011784) and Bi_5O_7I (COD 8104133). As expected, a clear pH-crystal phase dependence is observed. Through coprecipitation, pure BiOI was synthesized at pH 1 and 10; however, as the pH increases, peak broadening occurs, indicating a decrease in crystallite size. BiOI/Bi_5O_7I is combined at pH 12. Peak intensities indicate a higher proportion of BiOI in the mixture, and Bi_5O_7I is less crystalline than that achieved by itself. Single Bi_5O_7I is readily identified at pH 13 co-precipitation and hydrothermal synthesis. This pH-induced change in crystal phase is attributed to the gradual substitution of iodine atoms in BiOI by O atoms, which are originated from OH^- ions in the solution (Xiong et al. 2020). Crystallite sizes were estimated through Scherrer's equation

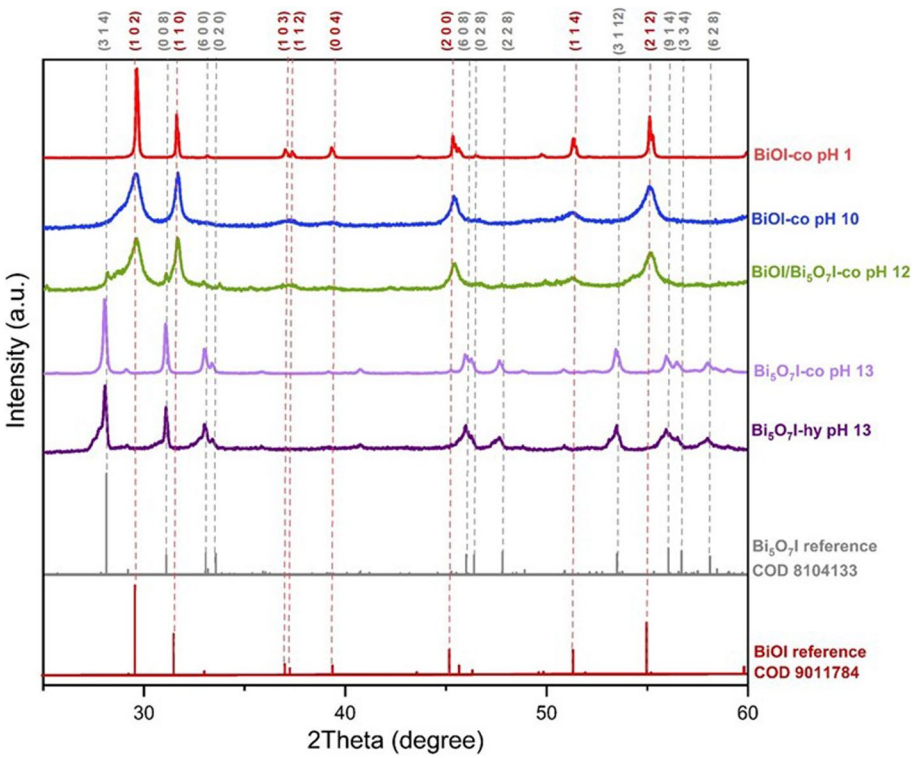

Fig. 1 XRD diffraction of the synthesized samples. Reference peaks for bismuth BiOI and Bi_5IO_7 with their corresponding Miller indices (h k l) are included

(Table 1). Observing comparable crystallite sizes for BiOI-co pH 1 and Bi_5O_7I (-co and –hy pH 13), with a decreased particle size for BiOI-co pH 10 and BiOI/Bi_5O_7I-co pH 12 as expected from the broaden XRD peaks. Peak asymmetries of BiOI-co pH 10 might be due to scattering or the geometry of the samples, and left/right asymmetry of BiOIs has been previously observed in literature (Jian and Hejing 2003; Reyna-Cavazos and A.M.-d. la Cruz, F.E. Longoria Rodríguez, E. López-Cuellar 2020).

To identify the elemental compositions of the bismuth oxyiodide samples, EDX results are given in Fig. S3. The Bi:O:I ratios for samples BiOI-co pH 1, BiOI-co pH 10, Bi_5O_7I-co pH 13, and Bi_5O_7I-hy pH 13 are congruent to the calculated elemental compositions (Fig. S3 inset data). In the case of BiOI/Bi_5O_7I-co pH 12, a Bi-O-I ratio of 2:2:1 is obtained, confirming the coexistence of BiOI and Bi_5O_7I species and indicating a higher proportion of BiOI in the mixture.

FTIR was performed to investigate the chemical composition and chemical bonding of the materials. As shown in Fig. S4, all of the synthesized bismuth oxyiodides have absorption peaks at 3400 and 1600 cm^{-1}, which may be due to the O–H bending vibration from adsorption of H_2O in the air by the material. Peaks at ≈1500 and 1384 cm^{-1} could be attributed to the vibrations of the Bi–O bond. The absorptions located around 400–700 cm^{-1} might correspond to the stretching vibrations of Bi–O, Bi–O–I, and Bi–O–Bi in bismuth oxyiodides (Wang et al. 2012; Lu et al. 2022; Lee et al. 2015; Xia et al. 2018). These peaks are best defined in the spectra of Bi_5O_7I (co and hy).

SEM micrographs in Fig. 2 display the varied morphologies of the synthesized bismuth oxyiodides. Sample BiOI-pH 1 in Fig. 2a display a stacked microsheets like structure, with single sheets of an estimated diameter of 2–3 µm, likely as secondary particle sizes. In contrast, BiOI-pH 10 is composed of microspheres with an estimated diameter of 2–5 µm with thin and bent nanosheets as elementary units (Fig. 2b). The size of the single sheets was significantly reduced. The BiOI compound exhibits distinct morphologies at pH values of 1 and 10, allowing for easy comparisons of performance without needing to consider other factors. Bi_5O_7I is composed of microneedles of 3–10 µm in length, observing a greater thickness when synthesized via hydrothermal procedure (Fig. 2d, e). BiOI/Bi_5O_7I-co pH 12 (Fig. 2c) shows the coexistence of both structural types, in accordance with the observed XRD patterns (Fig. 1). BiOI has previously been reported to have nanosheets and microspheres morphology (Hu et al. 2014), whereas Bi_5O_7I has microneedle structures (Cao et al. 2012).

In addition to the SEM analyses, TEM and HRTEM were performed to study the type of combination that occurred between BiOI and Bi_5O_7I in the BiOI/ Bi_5O_7I-co pH 12 sample (Fig. 3). As observed in the images, BiOI-co pH 10 has a microsphere structure (Fig. 3a), and Bi_5O_7I-co pH 13 shows long, highly crystalline microneedles (Fig. 3c). In the case of the sample with the coexistence of both structures (Fig. 3b), we notice that Bi_5O_7I microneedles are smaller and less crystalline, in accordance with XRD peaks. Moreover, HRTEM images of the sample reveal that these two microstructures are intricately entangled in a way that cannot be achieved through simple physical mixing, indicating that an heterojunction was achieved (Liao et al. 2021; Yu et al. 2024).

A considerable increase in the S_{BET} (Table 1) is observed from BiOI-co pH 1 (2 ± 1 m^2/g) to BiOI-co pH 10 (26 ± 1 m^2/g), in accordance with the diminished particle size apparent in the SEM images. BiOI/Bi_5O_7I-co pH 12 also presents 26 ± 1 m^2/g, while Bi_5O_7I display markedly reduced S_{BET} values through both co-precipitation and hydrothermal synthesis procedures. When compared to the benchmark TiO_2 P25, all of the bismuth oxyiodides samples exhibit significantly lower specific surface area (TiO_2 P25; S_{BET} = 43 ± 1 m^2/g). N_2 adsorption isotherms are depicted in Fig. S5. The isotherms are type IV according to the IUPAC classification, which were

Table 1 Characterization data

Sample	Eg (eV)	E_{CB} (V vs SHE)	E_{VB} (V vs SHE)	S_{BET} (m^2/g)	Pore diameter (nm)	PSD_{max} (µm)	Crystallite size (nm)
TiO_2 P25	3.1	−0.2	2.9	43 ± 1	13	0.025 (López Zavala et al. 2017)	17
BiOI-co pH 1	1.8	−0.1	1.7	2 ± 1	8	14	53
BiOI-pH 10	1.9	−0.1	1.7	26 ± 1	20	8/237	7
BiOI/Bi_5O_7I-co pH 12	1.9	-	-	26 ± 1	22	6/110	16
Bi_5O_7I-co pH 13	3.1	−0.3	2.8	2 ± 1	14	8	41
Bi_5O_7I-hy pH 13	3.1	−0.3	2.8	1 ± 1	9	10	39

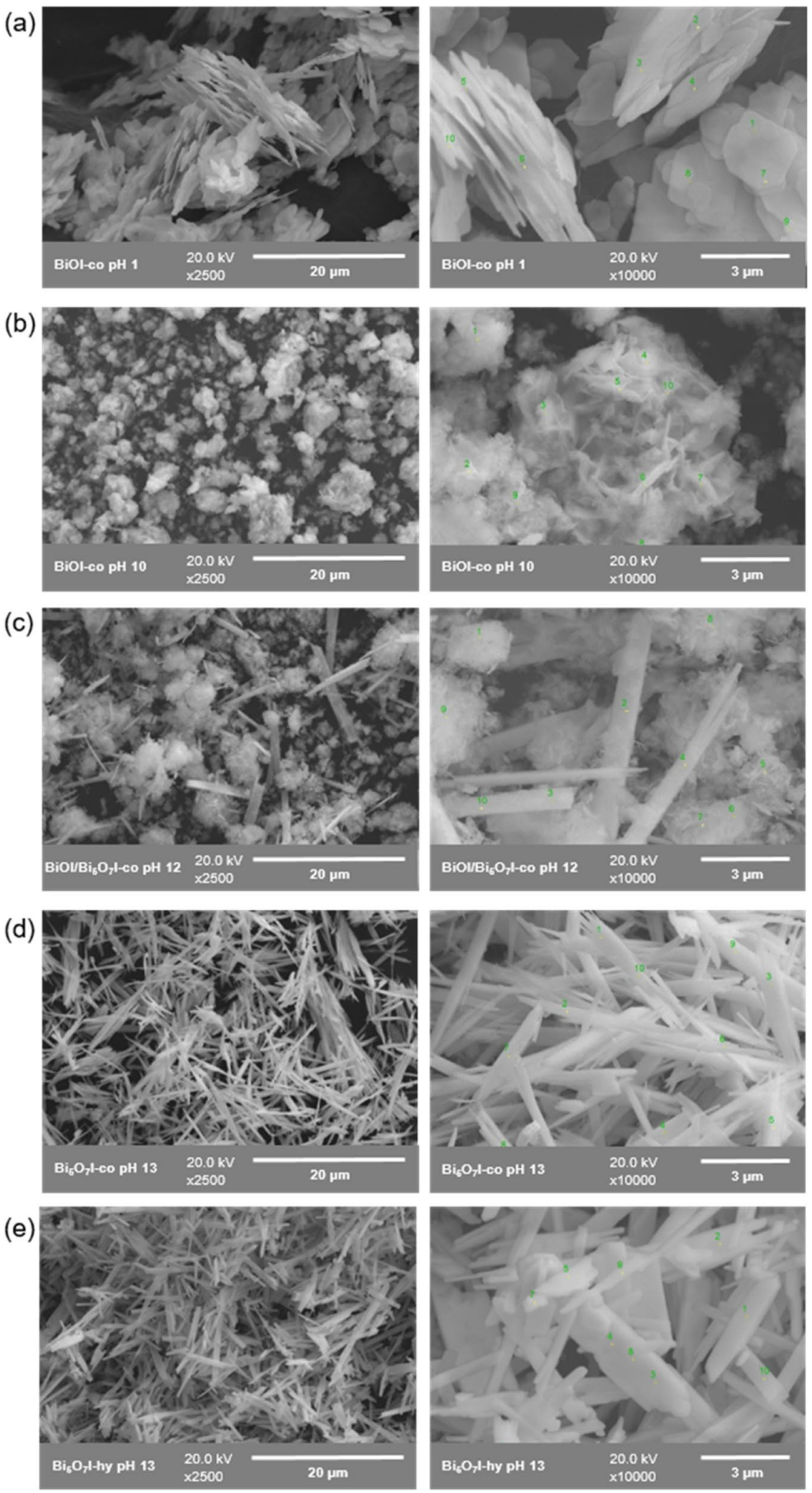

Fig. 2 SEM images of the synthesized **a** BiOI-co pH 1, **b** BiOI-co pH 10, **c** BiOI/Bi_5O_7I-co pH 12, **d** Bi_5O_7I-co pH 13, and **e** Bi_5O_7I-hy pH 13

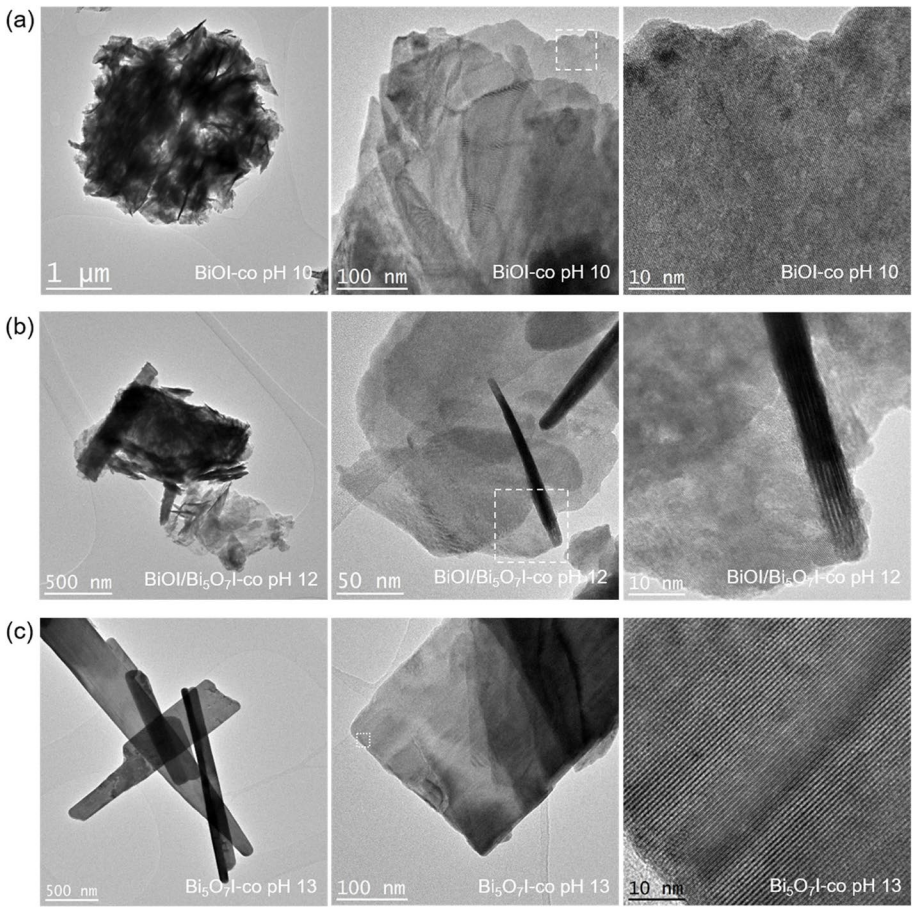

Fig. 3 TEM and HRTEM images of the synthesized **a** BiOI-co pH 10, **b** BiOI/Bi_5O_7I-co pH 12, and **c** Bi_5O_7I-co pH 13

characteristics of the mesoporous materials. BiOI-co pH 10 and BiOI/Bi_5O_7I-co pH 12 present H3 hysteresis loop, whereas the rest of the catalysts show a rather small and almost no hysteresis loops. The pore size distributions (Fig. S5) of BiOI-co pH 1, BiOI-co pH 10, and BiOI/Bi_5O_7I-co pH 12 displayed high amount of mesopores, in the range of 2–20 nm, and showed two peaks of small and large pores that can be attributed to the inter-nanosheet spaces, intrinsic porosity of the nanoparticles, and inter-particles spaces, respectively. In the case of Bi_5O_7I-co pH 13, along with its significantly lower S_{BET}, there is also a rapid decrease in its pore diameter. Bi_5O_7I-hy pH 13's pore size distribution curve is turned into a line indicating pores disappearance. This could be related with its microneedle structure and might have a negative impact on the photocatalytic performance of the photocatalyst (Hao et al. 2012; Gao et al. 2015; Ngo et al. 2024).

The particle size distribution profiles obtained from the bismuth oxyiodides confirmed the micro-size of the synthesized materials (Fig. 4). Maximum peak values (PSD_{max}) of particle size are recorded in Table 1. BiOI-co pH 1, Bi_5O_7I-co pH 13, and Bi_5O_7I-hy pH 13 present a size distribution profile ranged from 0.5 to 200 μm, with PSD_{max} of 14, 8 and 10 μm, respectively. The slight differences in the PSD_{max} values of Bi_5O_7I (-co and -hy) are comparable to the microneedles thickness variation observed in SEM images. BiOI-co pH 10 and BiOI/Bi_5O_7I-co pH 12 exhibit a double-peak profile.

Optical properties

Figure 5a shows the DR UV–Vis spectra of the bismuth oxyiodides samples with photographs of the colored powders reported as insets. TiO_2 P25 was also included for comparison. The light absorption edges are red-shifted with the color of the sample powders changing from white (TiO_2 and Bi_5O_7I), to orange (BiOI-co pH 10 and BiOI/Bi_5O_7I-co pH 12) and brown (BiOI-co pH 1). Both BiOI samples show absorption in the UV as well as visible portion of the electromagnetic spectrum; however, BiOI-pH 10 exhibits a much larger absorbance capability. Interestingly, Bi_5O_7I, synthesized through either procedure (coprecipitation or hydrothermal), shows only UV absorption. The lack of visible light absorption can be the consequence of a cathodic shift and/or anodic shift of the

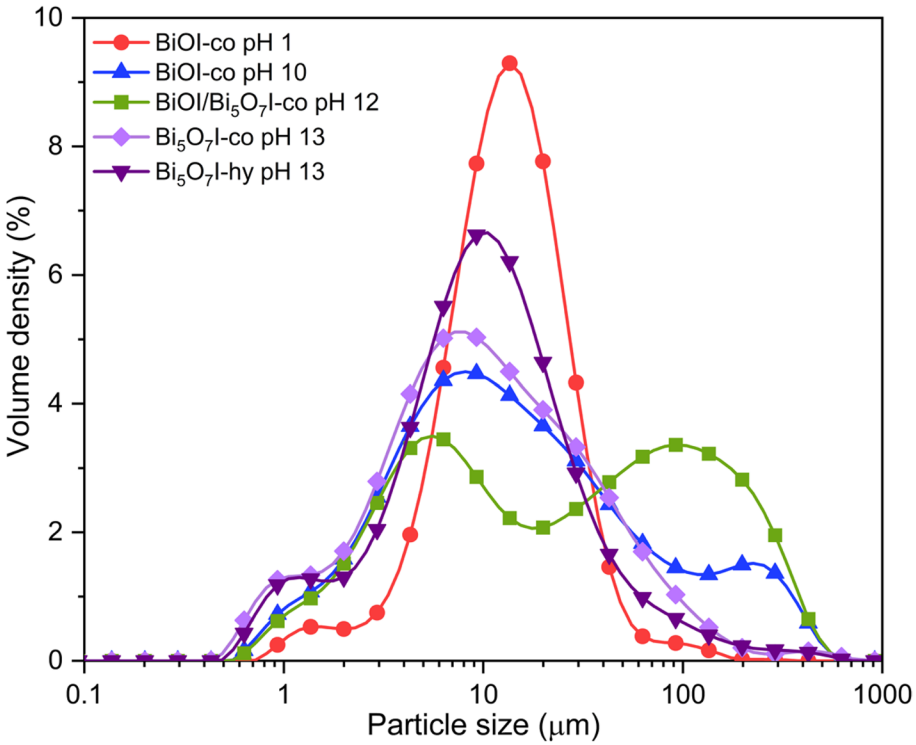

Fig. 4 Laser particle size distribution graphs from the synthesized bismuth oxyiodides

CB and VB edges respectively, when compared to BiOI, resulting in a larger band gap. This further demonstrates the possibility of tuning CB and VB edge redox potentials, as well as the band gap of the resulting material, by varying the Bi:I ratio during synthesis. Finally, the mixture BiOI/Bi_5O_7I showed an absorption profile, which, as expected, is (within experimental errors) equivalent to the one of BiOI-pH 10.

Tauc plot analysis (Makuła et al. 2018) reported in Fig. 5b was used to derive an estimation of the energies associated with indirect optical transitions between VB and CB. For this, the Kubelka–Munk function ($F(R_\infty)$) determined from the diffuse reflectance spectra was used, $(F(R_\infty)\cdot h\upsilon)^{1/2}$ vs. hυ were plotted, and the band gap energy (E_g) was obtained from the *x*-axis intersection. The extrapolated values are reported in Table 1. The values obtained here for the optical band gaps of BiOI and Bi_5O_7I matched what was previously reported for these materials (Yang et al. 2018; Martinez-Topete et al. 2025; Hassan et al. 2022).

Mott-Schottky plots (vs Ag/AgCl, 3-M KCl) for bismuth oxyiodides are given in Fig. 5c. The positive slope of the linear part of the $1/C^2_{SC}$ vs potential curve demonstrates that bismuth oxyiodides are *n*-type semiconductors. The obtained V_{fb} (V vs Ag/AgCl 3 M KCl) was converted to the standard hydrogen electrode (SHE) scale and assigned to the Fermi level (E_F) of the semiconductors (Eq. 1). E_F is considered as an approximation to E_{CB}, and E_{VB} is estimated using the value of the optical band gap (Table 1).

$$V_{fb}\ (\text{V vs SHE}) = V_{fb}\ (\text{V vs Ag/AgCl 3M KCl}) + 0.205\ (\text{V}) = E_F\ (\text{V vs SHE}) \quad (1)$$

Thus, the corresponding E_{CB} (V vs SHE) of samples BiOI-co pH 1, BiOI-co pH 10, Bi_5O_7I, and TiO_2 P25 were calculated to be −0.14, −0.13, −0.28, and −0.24 V, respectively. These values are similar to those obtained in prior publications (Liu and Wang 2016; Lin et al. 2019; Li and Wu 2015).

As shown in Fig. 5c, the VB of BiOI-co pH 1 and BiOI-co pH 10 exhibit similar positions (1.7 V), indicating that the differences in sample structures do not impact in the band position. The VB position of Bi_5O_7I (2.8 V), obtained through either synthetic method (coprecipitation or hydrothermal), is positively shifted compared with that of BiOI. This result suggests that the Bi-enrichment leads to a stronger oxidation ability of Bi_5O_7I, comparable to TiO_2 P25 (2.9 V).

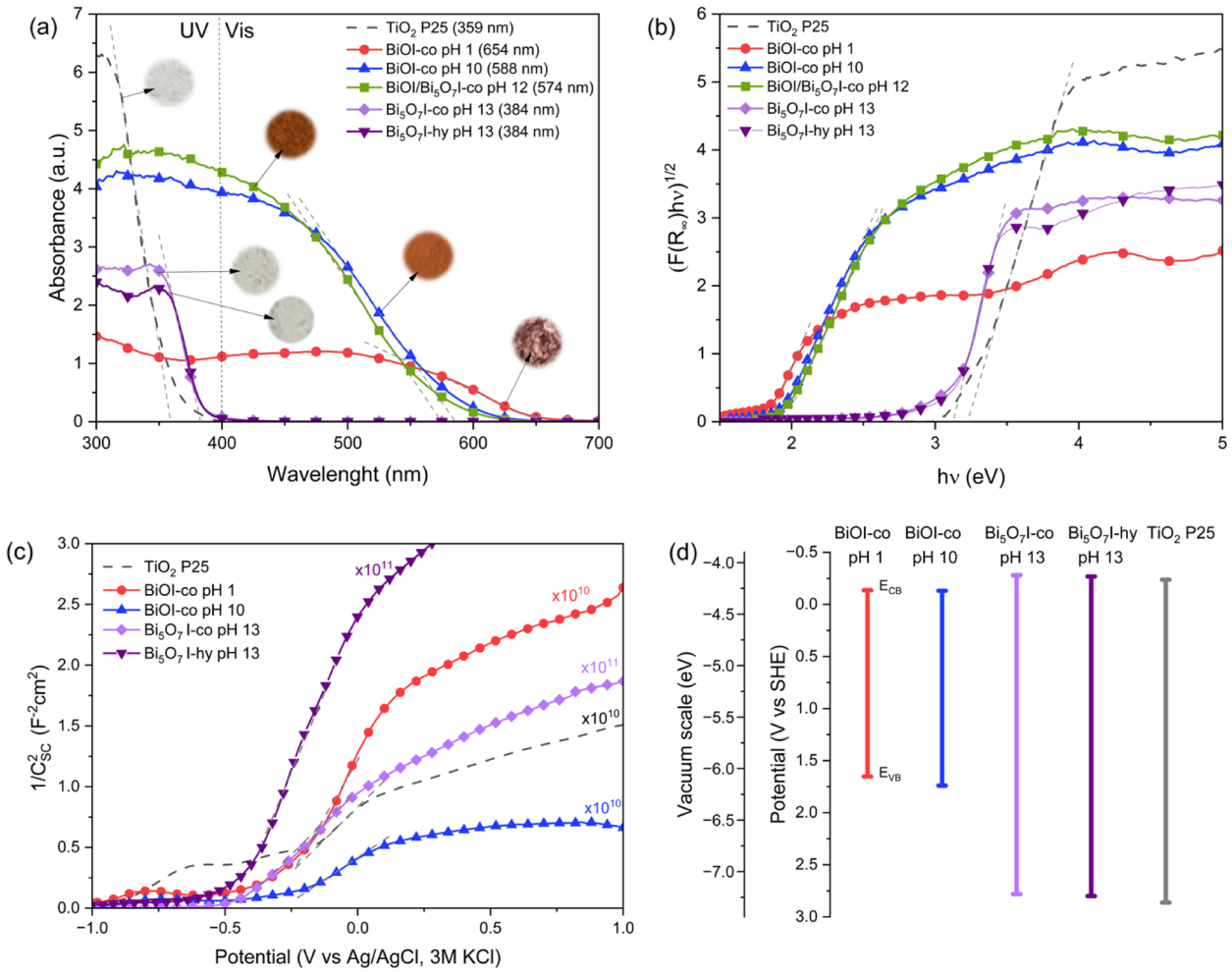

Fig. 5 **a** UV–Vis DRS spectra, **b** Kubelka–Munk plots of the bismuth oxyiodide samples, **c** Mott-Schottky plots, and **d** schematic electronic band structure diagram. The inset of **a** shows photographs of samples

PL spectra (Fig. 6) of the photocatalysts were recorded to study photogenerated charge carrier recombination. It is known that the higher the PL intensity, the greater the probability of charge recombination (Jimenez-Relinque et al. 2024; Pallotti et al. 2017). When comparing BiOI-co at pH 1 and pH 10, the recombination probability decreases considerably as the pH of the synthesis is increased, which highlights the role of the sample's structure in terms of the charge carrier separation. Bi_5O_7I exhibits a high recombination probability, while BiOI-co pH 10 and BiOI/Bi_5O_7I's are significantly lower than the rest. It is surprising that Bi_5O_7I, which has a similar band structure as TiO_2 P25, exhibits a substantially stronger recombination signal. BiOI/Bi_5O_7I material has the lowest recombination, which could indicate that this combined structure enhances light harvest and more effectively separates photogenerated e^--h^+ pairs.

Photocatalytic performance and intermediate product formation

Photocatalytic degradation of NO_x

Figure 7 illustrates the efficiency of NO/NO_x removal, NO_2 formation, and NO_3^- selectivity (SNO_3^-) for the synthesized bismuth oxyiodides under both UV (Philips BLB 15 W; 10 ± 1 W/m^2) and visible (Philips Master TL-D 15W with filter up to 425 nm; 15 ± 1 W/m^2) light irradiation (spectra of the lamps are given in Fig. S2). Under UV irradiation, TiO_2 P25 demonstrates the best NO degradation efficiency, followed by BiOI/Bi_5O_7I-co pH 12≈Bi_5O_7I-co pH 13, Bi_5O_7I-hy pH 13, and BiOI-co pH 10. BiOI-co pH 1 shows the lowest NO conversion efficiency. Bismuth-based oxyiodides have in general lower selectivity (higher NO_2 generation) than TiO_2 P25. The lower-than expected performances might be attributed to high recombination rates (BiOI-co pH 1 and Bi_5O_7I) (Fig. 6) and the overall low BET surface areas (Table 1).

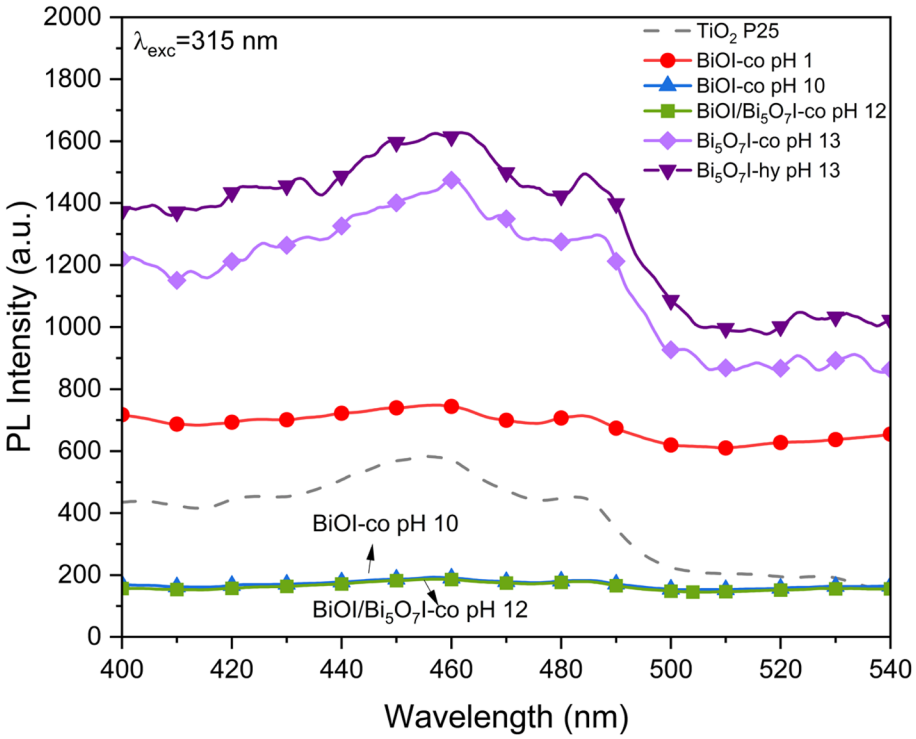

Fig. 6 Photoluminescence spectra (λ_{exc} = 315 nm) of bismuth oxyiodides samples. TiO_2 P25 was also included for comparison

Different ROS generation between TiO_2 P25 and the synthesized catalyst cannot be discarded. Under visible light, BiOI-co pH 10 and BiOI/Bi_5O_7I-co pH 12 are nearly twice as efficient at purifying NO air as the benchmark TiO_2 P25. Attributed to the lowered E_g (≈1.9 eV) and therefore an enhanced visible light absorption. In the case of BiOI (pH 1 vs pH > 10), a clear performance improvement is seen for the microsphere morphology (Fig. 2). However, as it exhibits a high NO_2 formation rate (low nitrate selectivity), the resulting NO_x degradation rates are comparable.

Photocatalytic decomposition of phenol

Figure 8a illustrates the phenol degradation efficiency as a function of reaction time under UV (Philips PLL UV-A 18W; $I = 20 \pm 2$ W/m^2 and 253 ± 1 photons/s/m^2) and visible light (white LED; $I = 800 \pm 80$ W/m^2 and 3372 ± 10 photons/s/m^2) (spectra of the lamps are given in Fig. S2). The removal efficiency is notably improved in the presence of TiO_2 solely under UV light. Conversely, under visible light irradiation, BiOI-co pH 10 and BiOI/Bi_5O_7I-co pH 12 exhibit a promising photocatalytic activity, five times greater than that of the TiO_2 P25 benchmark.

TiO_2 P25 achieved complete conversion after 180 min under UV light. Bi_5O_7I-hy and Bi_5O_7I-co pH 13 showed a degradation of almost 60%, while the other synthesized bismuth oxyiodides degraded less than 50%. On the other hand, when exposed to visible light, BiOI-co at pH 10 and BiOI/Bi_5O_7I-co pH 12 exhibit a promising 51% phenol degradation after 180 min, whereas the remaining bismuth oxyiodides (BiOI-co pH 10, Bi_5O_7I-co and -hy pH 13) and TiO_2 P25 catalysts show degradation of less than 30%.

To further understand the reaction kinetics of phenol degradation, the apparent pseudo-first-order model $ln(C_0/C) = Kt$ is applied to the experiments (Guillard et al. 1999).

The first-order linear fit data is shown in Fig. 8b, including the coefficient of determination (R^2). The R^2 values obtained for the different bismuth oxides analyzed ($R^2 > 0.87$) suggest a reasonably good linear fit for $ln(C_0/C)$ vs time, obtaining representative kinetic constant (K) values. TiO_2 under UV light presents the highest rate constant value (0.024 min^{-1}), followed by both Bi_5O_7I crystal structures (co and hy), which are much higher than those of the other bismuth oxyiodides. Under visible light, both BiOI-co at pH 10 and BiOI/Bi_5O_7I-co pH 12 reach maximum degradation rates of 0.004 min^{-1}, which are four times higher than the other materials.

To get some insight about the reaction mechanism scheme for phenol degradation using bismuth oxyiodides, the evolution of the total conversion of phenol

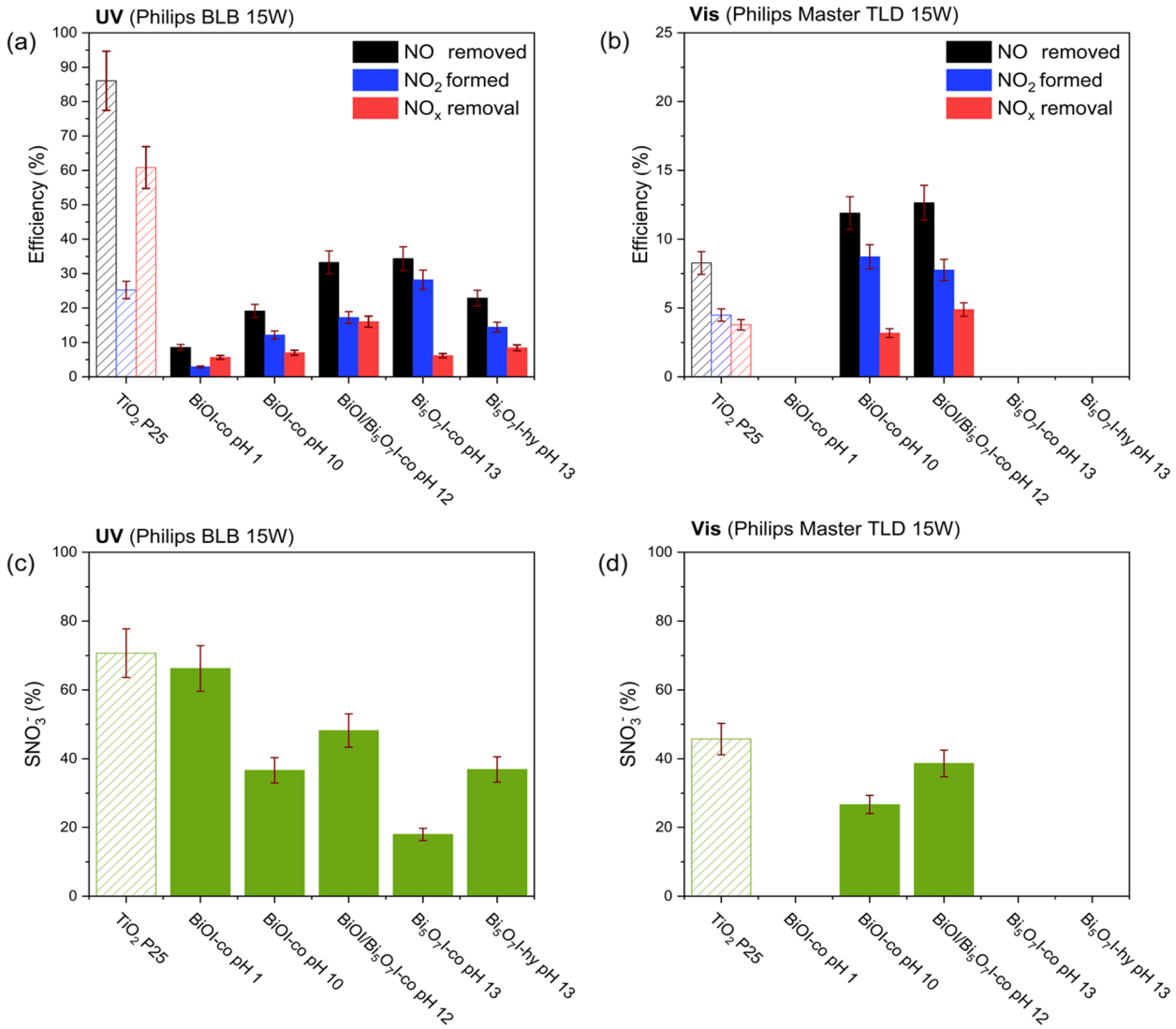

Fig. 7 NO, NO_2, and NO_x efficiency under **a** UV and **b** visible irradiation and nitrate selectivity (SNO_3^-) under **c** UV and **d** visible light

(TTG) and yield (TTI) (Eqs. 2–3) of possibly formed intermediates (hydroquinone, benzoquinone, and catechol) were calculated and compared to TiO_2 P25.

$$\mathrm{TTG}(\%) = \frac{[Ph]_0 - [Ph]_t}{[Ph]_0} \cdot 100 \tag{2}$$

$$\mathrm{TTI}(\%) = \frac{[Int]_t}{[Ph]_0} \cdot 100 \tag{3}$$

In Eq. 2, $[Ph]_0$ (μM) and $[Ph]_t$ (μM) represent the concentrations of organic pollutant after the surface of the photocatalysts had reached adsorption–desorption equilibrium and after light irradiation, respectively. In Eq. 3, $[Int]_t$ (μM) corresponds to the concentration of an intermediate compound at time t and $[Ph]_0$ (μM) to the initial concentration of phenol (Turki et al. 2015).

The evolution of the total conversion of phenol and yield of hydroquinone generation of all active samples is shown in Fig. 9. Benzoquinone and catechol signals are not detected. In comparison with TiO_2 P25, only traces of hydroquinone are formed in the presence of bismuth oxyiodides.

Additional tests using ^{1}H NMR spectroscopy were recorded to confirm that all of the intermediate organic reaction products during phenol degradation were identified (Fig. 10b). The type of irradiation used during testing was selected by whether the catalysts were UV or visible light responsive. In these experiments, the irradiation sources were UV (Philips Actinic BL 15 W;

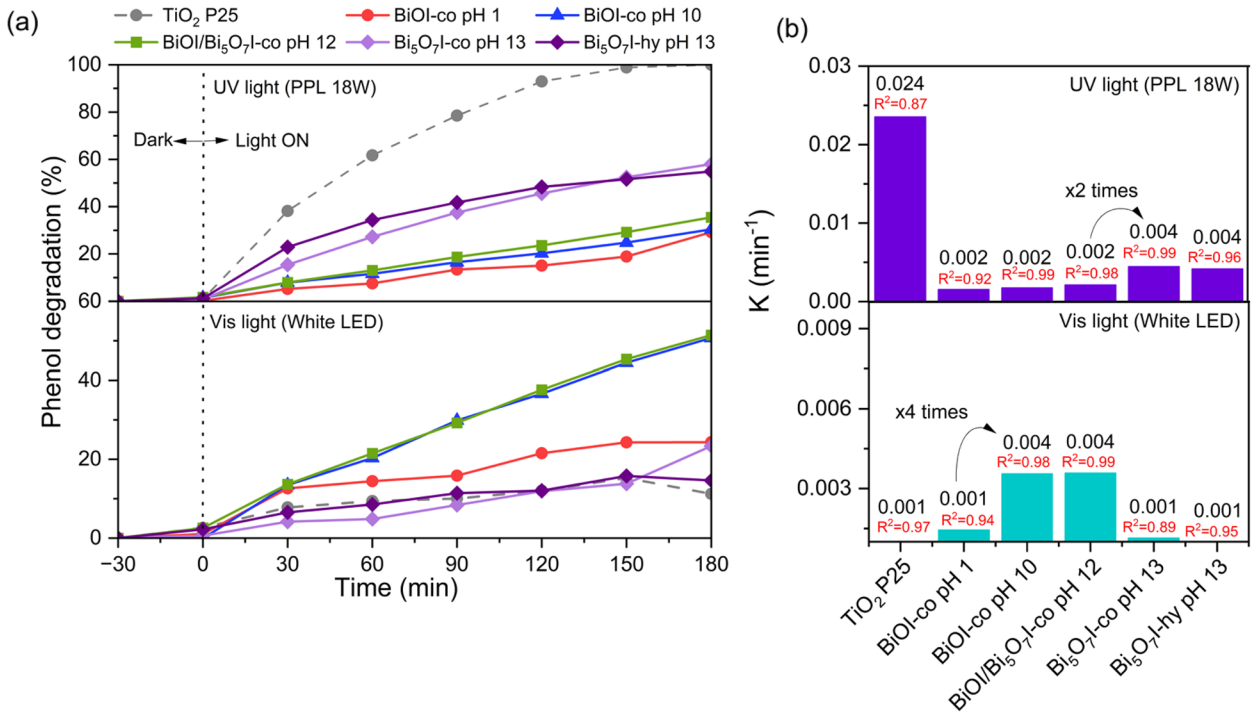

Fig. 8 **a** Phenol degradation results over different catalysts under UV and visible light irradiation and **b** the corresponding degradation rate constants. UV (Philips PLL UV-A 18W) or visible light (white LED)

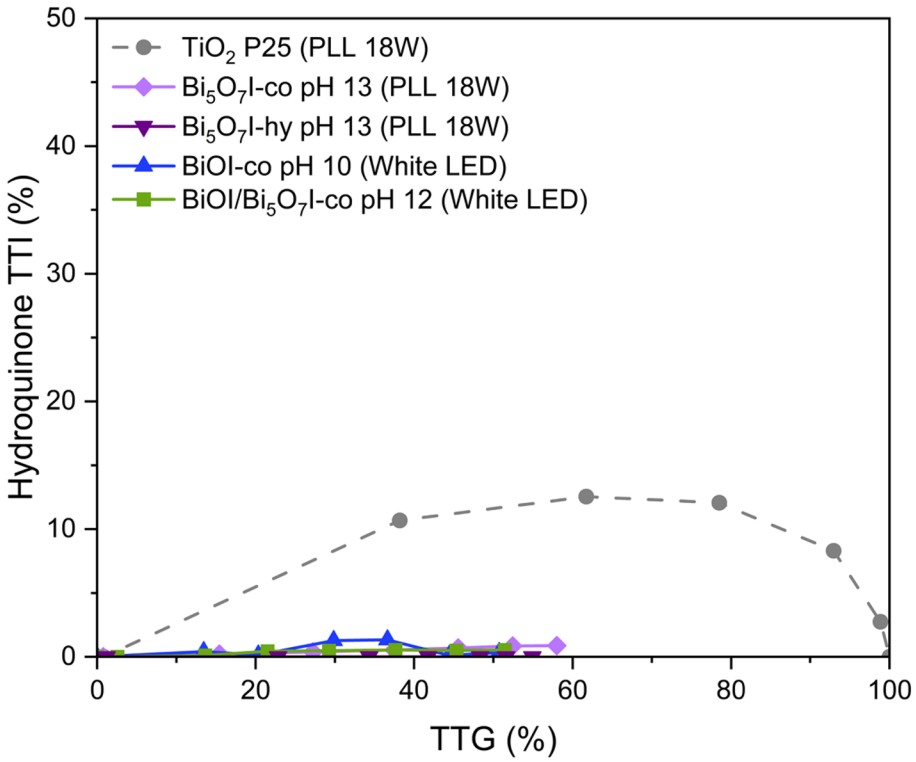

Fig. 9 Evolution of the yield of hydroquinone generation vs global conversion of phenol under both UV and visible irradiation conditions of all active samples. The type of light source (UV-PLL 18W or visible-white LED) was decided based on the maximum phenol degradation efficiency results

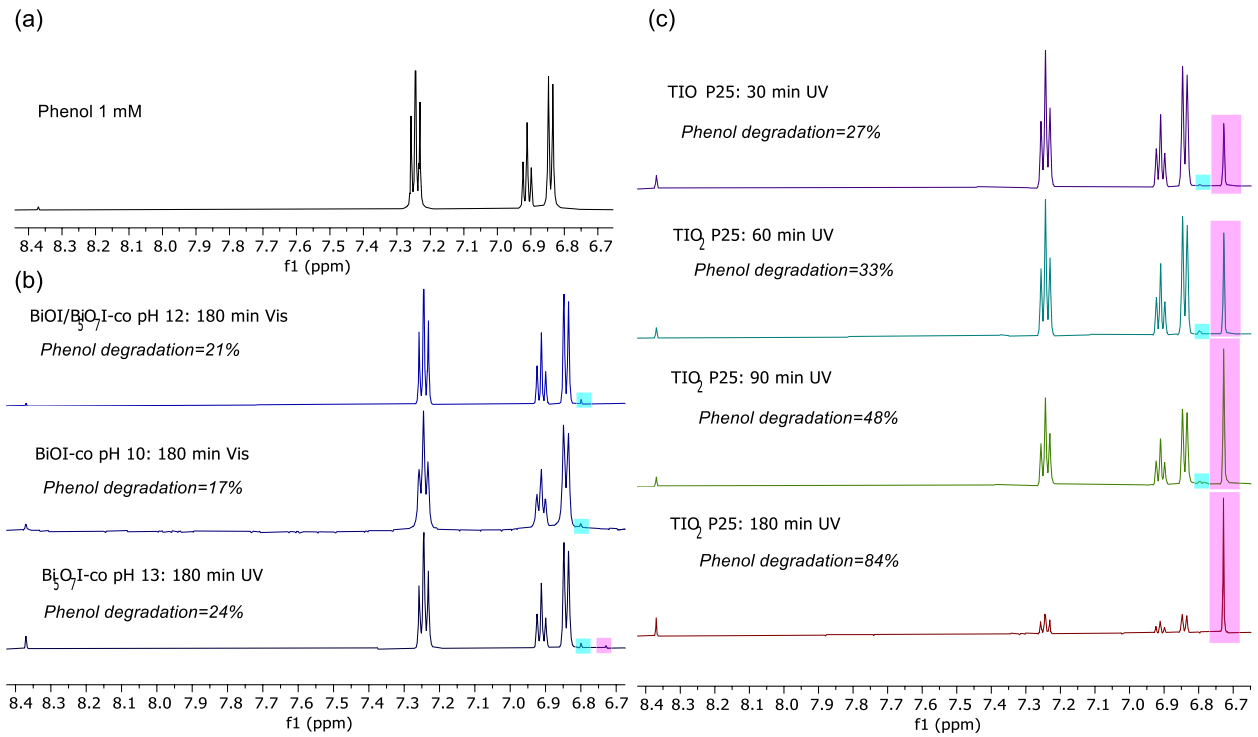

Fig. 10 Aromatic region of the.[1]H NMR (600 MHz, D_2O) spectra of **a** phenol, **b** photodegradation of phenol over different BiOI/Bi_5O_7I-co pH 12, BiOI-co pH 10, and Bi_5O_7I-co pH 13 photocatalysts after 180 min of UV (Philips Actinic BL 15 W) or visible (Philips Master TL-D 15W) irradiation, and **c** photodegradation of phenol as a function of UV irradiation time over TiO_2 P25

$I = 20 \pm 2$ W/m^2) or visible (Philips Master TL-D 15W; $I = 76 \pm 2$ W/m^2). Phenol spectrum data is depicted as reference (Fig. 10a). To obtain proton spectra at similar phenol degradation percentages for both TiO_2 and bismuth oxyiodides, TiO_2 from low irradiation times of 30 min to 180 min (Fig. 10c).

In order to detect a higher amount of intermediates, these experiments were carried out with irradiation sources of lower light intensity than those used in previous tests, with irradiances of 20 ± 2 and 76 ± 2 W/m^2, for UV and visible light respectively. Therefore, as expected, catalyst performance under these irradiation conditions is lower. The phenol degradation values obtained are depicted in Fig. 10. In all cases, the spectral appearance of new peaks confirms the formation of intermediates (Fig. 10b, c). All catalysts, bismuth oxyiodides and TiO_2 P25 (except TiO_2 P25 at higher irradiation time, 180 min), show a new singlet peak at $\delta = 6.79$ ppm (blue), which could belong to 1,4-benzoquinone traces (Turki et al. 2015; Hirakawa et al. 2002). The non-detection of 1,4-benzoquinone by HPLC may be attributed to the concentration being below the detection limit. TiO_2 P25 exhibits an additional singlet peak at $\delta = 6.72$ ppm (pink), possibly attributed to hydroquinone (Liu and Wang 2016). The most active bismuth oxyiodide sample, Bi_5O_7I-co pH 13, is the only one that exhibits this tiny peak. This is in accordance with the previously reported hydroquinone traces detected by HPLC.

The identification of intermediate compounds using HPLC and ^{1}H NMR may suggest that bismuth oxyiodides, regardless their composition and morphology, have a distinct mechanism of phenol degradation than TiO_2 P25 (Turki et al. 2015). However, the possibility of significant adsorption of hydroquinone onto bismuth oxyiodide materials cannot be neglected.

The photocatalytic degradation of organic pollutants usually leads to the decomposition of structure and eventually mineralization to CO_2 and H_2O, which can be visualized by the decrease of TOC. To assess the extent of mineralization during photocatalytic degradation of phenol, TOC values of the best-performing samples (under both irradiation conditions) have been obtained after 180-min irradiation using the same irradiation sources (Fig. 11). Following UV light irradiation, the TOC reduction was 57%, 42%, and 31% for TiO_2 P25, Bi_5O_7I-co pH 13 and Bi_5O_7I-hy, respectively. Conversely, under visible light exposure, BiOI-co pH 10 and BiOI/Bi_5O_7I-co pH 12 exhibited reductions of approximately 6% and 9%, respectively.

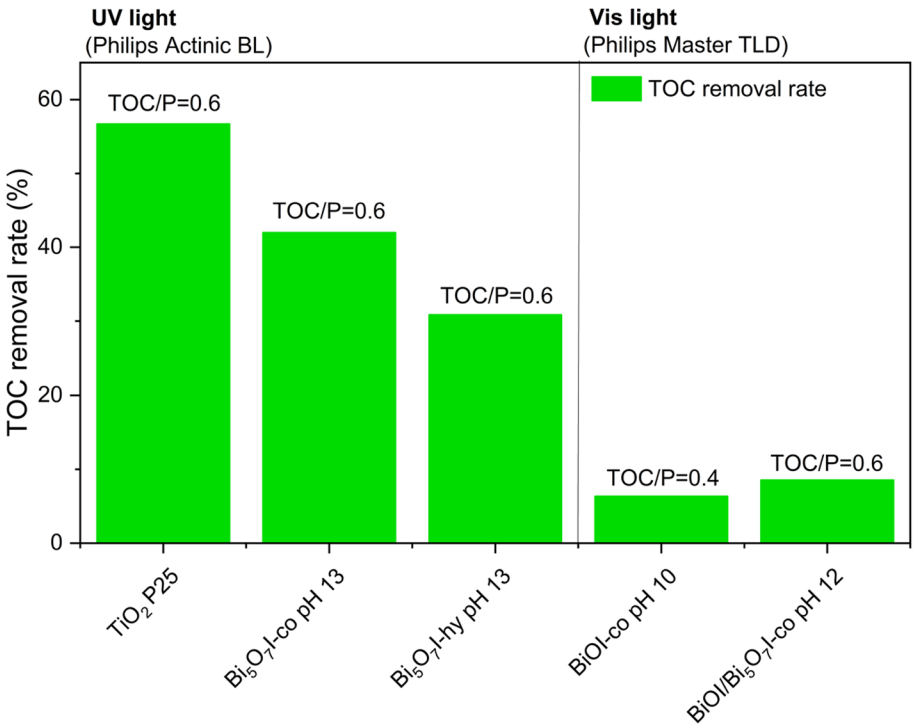

Fig. 11 TOC removal rates for the selected samples with best performance. Calculated ratios TOC/P are included. UV (Philips Actinic BL 15 W) or visible (Philips Master TL-D 15W) irradiation

To favor the comparability of the results, ratios between TOC removal rate $\left(\mu molL^{-1}\right)$ and phenol degradation rate $\left(\mu molL^{-1}\right)$ were calculated (TOC/P) (Eq. 4). TOC/P ratios of 0.6 were obtained for TiO_2 P25, Bi_5O_7I-co pH 13, and Bi_5O_7I-hy under UV exposure. Excited by visible light, BiOI-co pH 10 and BiOI/Bi_5O_7I-co pH 12 ratios of 0.4 and 0.6 were found, respectively. These ratio results indicate that Bi_5O_7I-UV, BiOI/Bi_5O_7I-VIS, and TiO_2 P25-UV systems have comparable mineralization capabilities.

$$\mathrm{TOC/P} = \frac{TOC\ dissapeared\ (\mu molL^{-1})}{Phenol\ degraded\ (\mu molL^{-1})} \tag{4}$$

Reusability tests

The stability of the best-performing samples under both irradiation conditions was further evaluated by cycle tests (Fig. 12). The phenol photocatalytic degradation was reproducible in three consecutive 180 min irradiation experiments, thus demonstrating the stability of these catalysts. For more clarity in the results, the degradation of the first cycle was normalized to 100% for all samples.

Factors affecting photocatalytic activity of bismuth oxyiodides samples and elucidation of reactive oxygen species (ROS) photocatalytic degradation pathways

To facilitate the discussion of photocatalytic activity results, Fig. 13 compares the photocatalytic performance for NO_x and phenol (%) for all samples under both UV and visible irradiation conditions. Overall, NO and phenol photodegradation rates show a similar trend, and slight deviation of results can be attributable to comparability of different classes of environmental remediation applications on different media (aqueous solution and air). For example, the lack of activity for NO_x removal under visible light for the BiOI-co pH 1, Bi_5O_7I-co pH 13, and Bi_5O_7I-hy pH 13 samples could be attributed to the distinct nature of the reaction media (Balázs et al. 2011). In the case of phenol, which is in aqueous phase, its higher solubility and ability to adsorb onto the photocatalyst surface facilitate the interaction with the catalyst. This allows the photocatalyst to generate the necessary reactive species for efficient degradation. On the other hand, the removal of NO_x in the gas phase presents additional challenges. Gaseous contaminants, like NO_x, tend to have lower adsorption efficiencies on the photocatalyst surface compared to aqueous compounds. Additionally, NO oxidation requires specific conditions, such as an appropriate band positions or reactive oxygen species

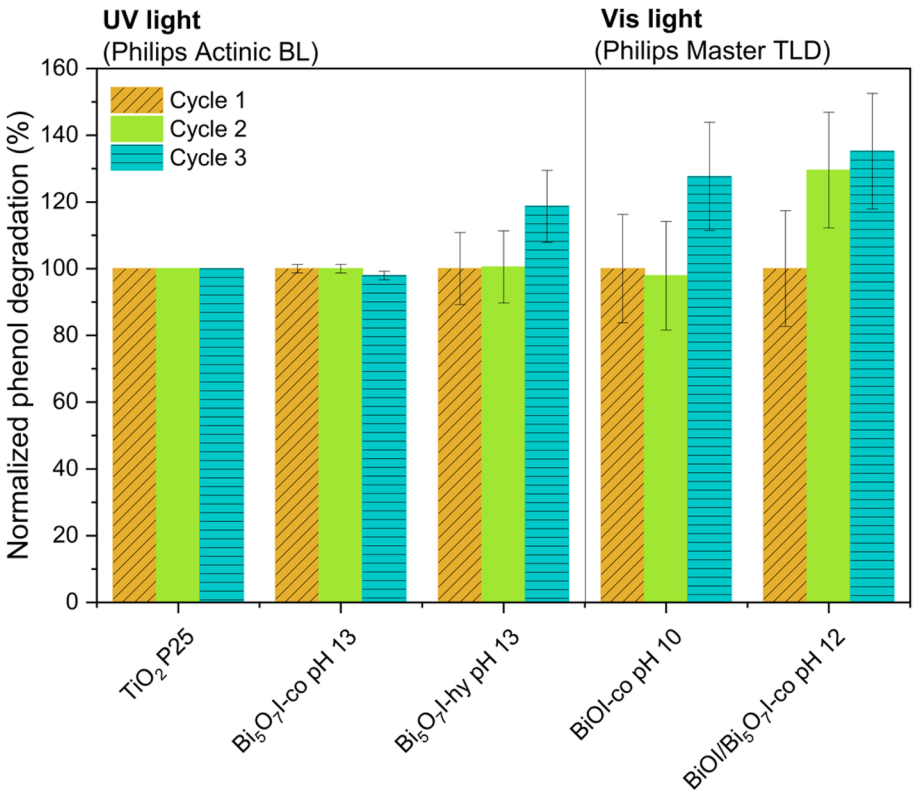

Fig. 12 Phenol reusability tests for the selected samples with best performance under UV (Philips Actinic BL 15 W) or visible (Philips Master TL-D 15W) irradiation conditions

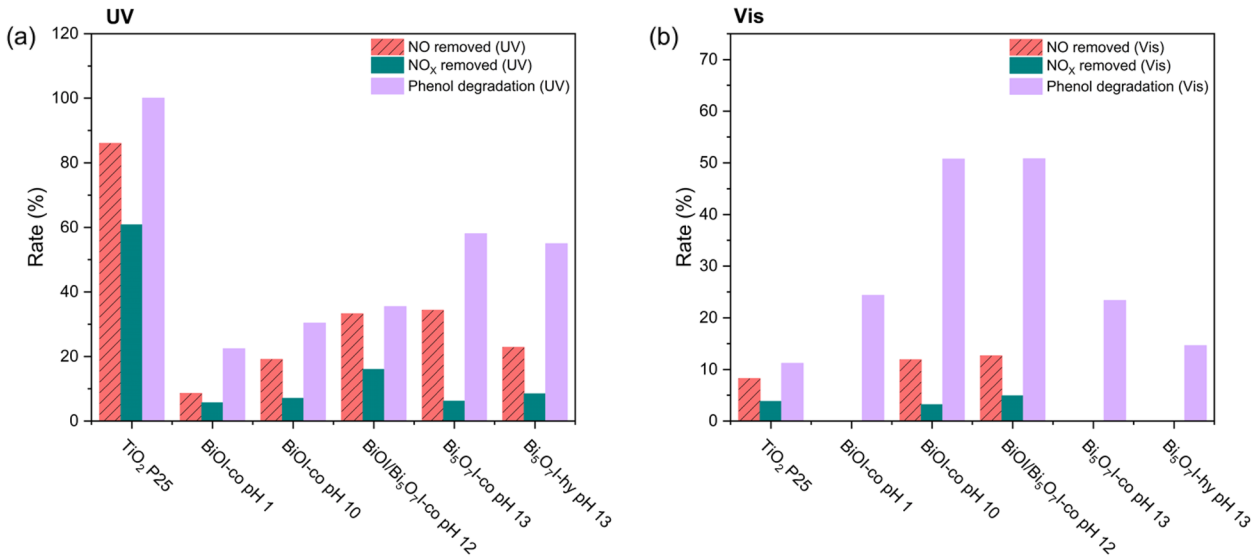

Fig. 13 Comparison of phenol degradation (180 min of irradiation) and NO and NO_x (30 min of irradiation) removal rates for all samples under **a** UV and **b** visible light irradiation

that might be different than those required for phenol degradation, and may be less effective under visible light for the studied photocatalysts. Indeed, a similar trend was observed in a previous work, where BiOX samples exhibit different photocatalytic efficiencies for phenol degradation and NO_x oxidation (Jimenez-Relinque et al. 2024).

In this work, two BiOI samples (BiOI-co pH 1 and BiOI-co pH 10) were prepared. These two materials have similar band structures (Fig. 5d, Table 1), with narrow band gap energy (1.8–1.9 eV) and band potentials (E_{CB} = −0.1 V and E_{VB} = 1.7 V). However, the lower photocatalytic performance (NO and phenol removal) of BiOI-co pH 1 under both irradiation conditions can be attributed to its smallest BET surface area (2 ± 1 m^2/g). This is associated with its micro-sheet stacked structure. In contrast, BiOI-co pH 10 sample had a larger S_{BET} area (26 ± 1 m^2/g) related to an open nanosheet-composed microspheres structure, which resulted in an increased photocatalytic performance. Furthermore, BiOI-co pH 10 reveals high light absorbance capability (Fig. 5a) and low e^--h^+ recombination rate (Fig. 6), which further contributes to this sample high reactivity in comparison with BiOI-co pH 1.

The formation of BiOI/Bi_5O_7I remains to match with visible light absorption (Fig. 5a). High BET surface area and low recombination rate are maintained (Fig. 6, Table 1). The enhanced photodegradation of NO and phenol (more perceptible under UV light) can be attributed to the presence of UV light-responsive Bi_5O_7I photocatalyst. Whereas the activity under visible light may be due to the presence of BiOI, considering the microsphere morphology, it is reasonable to obtain activities comparable to those of BiOI-co pH 10. Previous reports have highlighted potential enhancement of photocatalytic performance attributed to the formation of a heterojunction photocatalysts (Geng et al. 2024; Yu et al. 2015).

The as-prepared Bi_5O_7I materials via co-precipitation and hydrothermal procedures are UV-responsive photocatalysts with band gap of 3.1 eV. Generally, higher Bi content results in a wider band gap in oxyiodide compounds (Xiong et al. 2020; Jin et al. 2017). In regard to the band edge position, Bi_5O_7I exhibits a more cathodic conduction band (E_{CB} = −0.3 V) and a more anodic valence band (E_{VB} = 2.8 V), in comparison to BiOI. Interestingly, both prepared Bi_5O_7I shows a good VB position that provide a promising oxidation ability comparable to TiO_2 P25 (Fig. 5d). However, the photocatalytic performance is lower than expected. This limitation may be attributed to its low BET surface area (2 ± 1 m^2/g) and high recombination rate (Fig. 6). However, a different ROS-mediated mechanism of TiO_2 and bismuth oxyiodides compounds cannot be neglected.

Upon comparing the photocatalytic activities obtained for the different bismuth oxyiodides synthesized with those reported in the literature, a diverse range of results emerged. In Table 2, the results obtained in various studies from the literature are compiled, mentioning the morphology of the materials, the synthesis procedure, and the conditions of the photocatalytic activity tests to facilitate intercomparison. Just studies of catalysts with the same morphologies have been included. According to our knowledge, comparable BiOI/Bi_5O_7I as-prepared samples have not been used in any previous work, thus are not included. In addition, most of the results found in the literature correspond to experiments conducted solely under visible light irradiation. Despite differing synthesis methods, Jiménez-Relinque et al. (Jimenez-Relinque et al. 2024) and this study found similar both phenol and NO_x degradation results under UV (phenol = 20–22%; NO = 5–9%) and visible light (phenol = 24–25%; NO = 0–1%) for BiOI-microsheet structure samples. Discrepancies arise between the bibliographic results for BiOI with a microsphere structure under visible light. While Dong et al. (Dong et al. 2015) and Zhu et al. (Zhu et al. 2019) report superior NO degradation (60% and 33–45%, respectively), Wu et al. (Wu et al. 2017) record lower phenol activities (7% after 180 min), and Wang et al. (Wang et al. 2017b) yield comparable results to this study (53% after 180 min). Similarly, for Bi_5O_7I, phenol degradation results under visible light obtained by Wu et al. (Wu et al. 2017) and Gao et al. (Gao et al. 2020) align with this study (≈10–20%). However, the correct comparison of the absolute efficiencies obtained in the different works is difficult, due to the use of different lamps with emission peaks at different wavelengths and with different irradiance and/or photon flux values, which in the majority of the cases are not specified.

Regarding the formation of undesired by-products during the photocatalytic reactions, bismuth oxyiodide samples formed traces of detected typical intermediates during phenol decomposition and high NO_2 generation during NO_x removal in comparison with TiO_2 P25. The discrepancies of intermediate formation trend between tests may be due to unfavorable BV and CV potentials for the target reactions or phenol by-products being absorbed onto the catalyst surface that might affect the reaction selectivity. However, it is crucial not to overlook the possibility of a different ROS-mediated mechanism for TiO_2 and bismuth oxyiodide compounds.

Since ROS are primary intermediates of photocatalytic reactions, as previously stated, their identification is important in terms of understanding the photodegradation mechanisms. The HO·, which is produced at the metal oxide surface by the photocatalytic oxidation of H_2O with the VB holes (h^+), is often assumed to be the

Table 2 Comparison aspects of as-synthetized BiOI and Bi_5O_7I and photocatalytic performance with other previously reported studies

Sample	Morphology	Pollutant	Synthesis	Experimental procedure	Degradation rate	Refs.
BiOI	Microsheets	NO_x	Method: co-precipitation (r.t., 24 h) Solvent: H_2O pH: 1	500 ± 50 ppb NO and flow rate of 1 L/min	UV: NO 9% and NO_x 6% Vis: NO 0% and NO_x 0%	This work
			Method: grinding (r.t., 10 min) Solvent: - pH: -	1000 ± 50 ppb NO and flow rate of 0.5 L/min	UV: NO 5% and NO_x 4% Vis: NO 1% and NO_x 0%	(Jimenez-Relinque et al. 2024)
		Phenol	Method: co-precipitation (r.t., 24 h) Solvent: H_2O pH: 1	0.2-mM phenol, 1 g/L catalyst, 180-min irradiation	UV: 22% Vis: 24%	This work
			Method: grinding Solvent: - pH: -	0.2-mM phenol, 1 g/L catalyst, 180-min irradiation	UV: 20% Vis: 25%	(Jimenez-Relinque et al. 2024)
BiOI	Microspheres	NO_x	Method: co-precipitation (r.t., 24 h) Solvent: H_2O pH: 10 (NaOH)	500 ± 50 ppb NO and flow rate of 1 L/min	UV: NO 19% and NO_x 7% Vis: NO 12% and NO_x 3%	This work
			Method: hydrothermal (160 °C, 12 h) Solvent: ethylene glycol	600-ppb NO and flow rate of 1 L/min	Vis: NO 60%	(Dong et al. 2015)
			Method: hydrothermal (160–200 °C, 18 h) Solvent: ethylene glycol	430-ppb NO and flow rate of 4 L/min	Vis: NO 33–45%	(Zhu et al. 2019)
		Phenol	Method: co-precipitation (r.t., 24 h) Solvent: H_2O pH: 10 (NaOH)	0.2-mM phenol, 1 g/L catalyst, 180-min irradiation	UV: 30% Vis: 51%	This work
			Method: co-precipitation (70 °C, 5 min) Solvent: $H_2O + HNO_3$ Additive: PEG 6 K	0.2-mM phenol, 1 g/L catalyst, 240-min irradiation	Vis: 7% after 180 min and 12% after 240 min	(Wu et al. 2017)
			Method: hydrothermal (160 °C, 12 h) Solvent: methanol and ethylene glycol (1:1)	0.5-mM phenol, 1 g/L catalyst, 6-h irradiation	Vis: 53% after 180 min and 94% after 6 h	(Wang et al. 2017b)
Bi_5O_7I	Microneedles	NO_x	Method: co-precipitation Solvent: H_2O pH: 13 (NaOH)	500 ± 50 ppb and flow rate controlled at 1 L/min	UV: NO 34% and NO_x 6% Vis: NO 0% and NO_x 0%	This work
			Method: hydrothermal (160 °C, 24 h) Solvent: H_2O pH: ≈13 (NaOH)	500 ± 50 ppb and flow rate controlled at 1 L/min	UV: NO 23% and NO_x 8% Vis: NO 0% and NO_x 0%	This work
		Phenol	Method: co-precipitation Solvent: H_2O pH: 13 (NaOH)	0.2-mM phenol, 1 g/L catalyst, 180-min irradiation	UV: 58% Vis: 23%	This work
			Method: hydrothermal (160 °C, 24 h) Solvent: H_2O pH: ≈13 (NaOH)	0.2-mM phenol, 1 g/L catalyst, 180-min irradiation	UV: 55% Vis: 15%	This work
			Method: thermal treatment of BiOI (520 °C with 3 °C/min for 4 h)	0.07-mM phenol, 1 g/L catalyst, 150-min irradiation	Vis: 10%	(Gao et al. 2020)
			Method: co-precipitation (70 °C, 5 min) Solvent: $H_2O + HNO_3$ Additive: PEG 6 K pH: basic (NaOH)	0.2-mM phenol, 1 g/L catalyst, 240-min irradiation	Vis: 20% after 180 min and 33% after 240 min	(Wu et al. 2017)

major species responsible for the photocatalytic oxidative reaction.

To evaluate the role of this active specie during the photocatalytic reaction, isopropyl alcohol (IPA) as HO· quencher was introduced in the phenol degradation experiment carried out with Bi_5O_7I photocatalysts. This crystal structure was selected because the VB oxidation position is comparable to that of TiO_2 P25 (Fig. 5) and evaluation of Gibbs energy change (ΔG), calculated from $E^0(HO\cdot/H_2O) = 2.31$ V (Dang et al. 2016) and E_{VB}, showed that HO· generation is thermodynamically favored ($\Delta G < 0$). Figure 14 shows that adding IPA reduces phenol degradation by TiO_2 P25 when compared with that of no quencher whereas leaving Bi_5O_7I-co pH 13 and Bi_5O_7I-hy unaffected. This finding suggests that HO· are involved in the degradation mechanism of phenol by TiO_2 P25, but not over Bi_5O_7I, even though the holes on the VB of this compound are theoretically capable of oxidizing H_2O to produce HO·.

TA fluorescence probe experiments to measure HO· were also performed.

Jimenez-Relinque et al. 2017; Martinez-Topete et al. 2025; Jimenez-Relinque and Castellote 2018; Nosaka et al. 2003; Ishibashi et al. 2000). The reaction of generated HO· with TA forms TAOH, which presents a fluorescence peak at 425 nm (Fig. 15a). As observed in Fig. 13b, the FL intensity ($\lambda = 425$ nm) of TiO_2 increases with the UV irradiation time. Thus, HO· was produced through TiO_2. The loss of linearity in the increase of fluorescence intensity of TiO_2 may be attributed to the absence of enough available free TA probe to react. No TAOH was generated by Bi_5O_7I-co pH 13 nor Bi_5O_7I-hy pH 13 samples. This is solid evidence to confirm that HO· are invariably not the major oxidants produced in Bi_5O_7I photocatalysis.

To further ascertain the generation of HO· by TiO_2 P25 but not by Bi_5O_7I, spin-trap EPR experiments were conducted. We confirmed the generation of HO·/HOO· in UV-irradiated TiO_2 P25 (Fig. 16a) in the presence of DMPO. Figure 15a shows a 1:2:2:1 quartet of resonances typical of a DMPO-OH radical adduct where the unpaired electron of the aminoxyl moiety couples to the ^{14}N and the $^1H_\beta$ nuclei with identical isotropic hyperfine coupling constants (hccs) and equal to a_{iso} (^{14}N) = a_{iso} ($^1H_\beta$) = 1.49 mT. This spectrum is indicative of the trapping of HO· and, due to the photoreaction being conducted outside of the EPR resonator, potential direct trapping of $O_2{\cdot}^-$/HOO· (DMPO-OOH in water persists only for a few minutes before undergoing ring opening to a diamagnetic 4-methyl-4-nitroso-pentanal, releasing HO· that in the presence of excess DMPO forms DMPO-OH) (Finkelstein et al. 1982). In the case of Bi_5O_7I

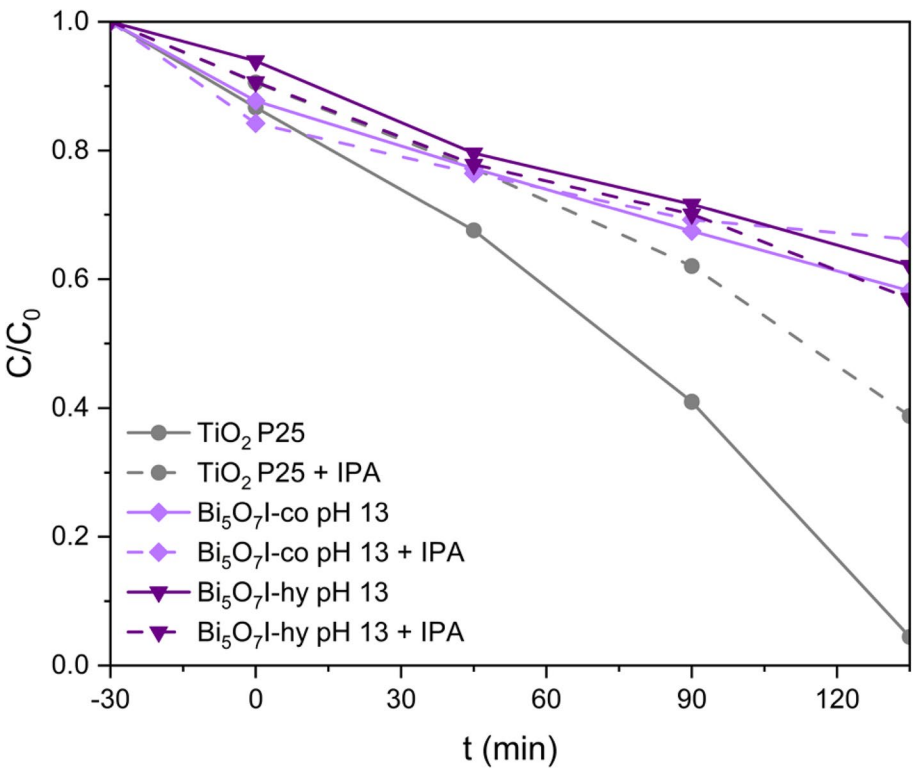

Fig. 14 Phenol degradation under UV light in the presence of IPA (HO· quencher)

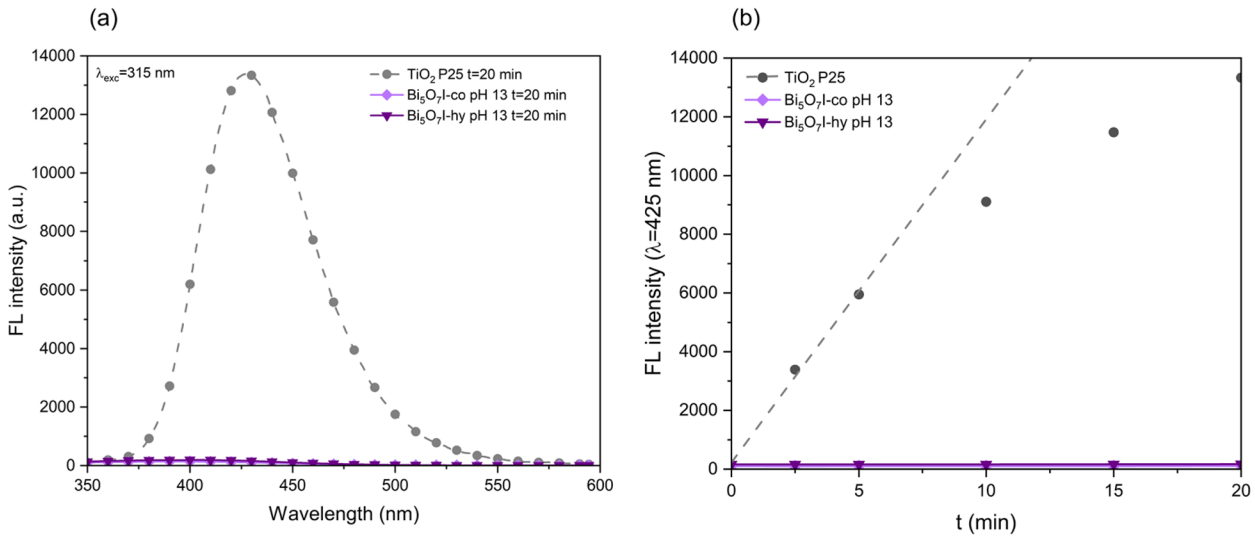

Fig. 15 **a** FL spectra (λ_{exc} = 315 nm) of TAOH over samples after 20 min of UV irradiation and **b** FL intensity linear fit of TAOH (λ = 425 nm) at different irradiation time

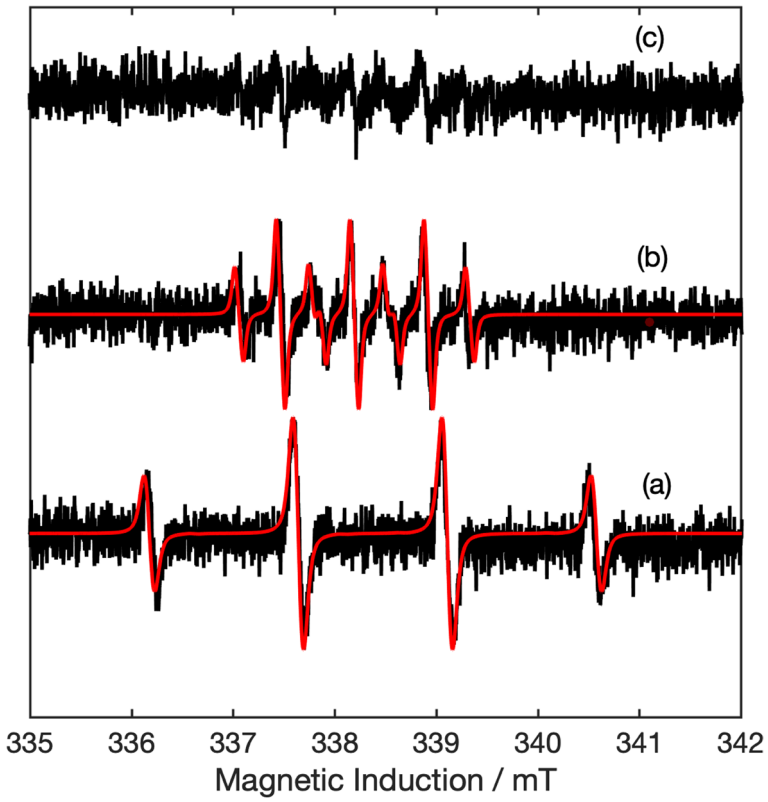

Fig. 16 X-band continuous wave (CW) EPR experimental spectra (black traces) and simulations (red traces) of **a** TiO_2 P25, **b** Bi_5O_7I-hy pH 13, and **c** Bi_5O_7I-co pH 13 in water suspension irradiated under UV light for 5 min with 30 mM DMPO

however (Fig. 16b, c), no hydroxyl or hydroperoxyl fingerprint was observed. On the contrary, spin trapping EPR revealed the presence of a nine-resonance line spectrum arising from the coupling of the unpaired electron to the ^{14}N nucleus of the aminoxyl moiety, a_{iso} (^{14}N) = 0.73 mT, and two identical $^{1}H_{\gamma}$ nuclei, $2 \times a_{iso}$ ($^{1}H_{\gamma}$) = 0.41 mT.

This spectrum is indicative of DMPOX oxidation product of the initial DMPO spin trapping reagent. DMPOX formation can occur when DMPO is oxidized by high-valent metals, by a sudden generation of a large amount of HO· or by $^1O_2$ (Kim et al. 2020; Zhu et al. 2020; Huang et al. 2022, 2018). A sudden generation of a large amount of HO· were previously excluded (Fig. 15). Otherwise, Bi_5O_7I photocatalysts would exhibit a greater UV photocatalytic efficiency than TiO_2 P25, which we showed it is not the case. Therefore, the formation of DMPOX must arise from either a higher metal oxidation state (Bi(V)) or singlet oxygen formation under UV irradiation. In both cases though, these species are less oxidative and reactive than HO·, which would partially explain the much lower photocatalytic efficiencies and selectivity of Bi_5O_7I when used to degrade phenol or NO_x. Additionally, in the case of phenol degradation, previous works have shown that singlet oxygen reacts with phenol exhibiting extreme selectivity toward the *para* position, leading to the formation of 1,4-benzoquinone as by-product, consistent with the previous results observed in the ^1H NMR spectra (Fig. 9) (J. Al-Nu'airat, B.Z. Dlugogorski, X. Gao, N. Zeinali, J. Skut, P.R. Westmoreland, I. Oluwoye, M. Altarawneh 2019), leading us to believe in the possibility of this potential degradation pathway.

Although all these experiments for ROS detection have been conducted in Bi_5O_7I, the absence of HO· formation can be extrapolated to the other BiOI samples. Evaluation of Gibbs energy change (ΔG), calculated from $E^0(HO^•/H_2O) = 2.31$ V (Koppenol et al. 2010) and E_{VB}, showed that HO• generation is not thermodynamically favored in the case of BiOI (ΔG > 0). Based on the aforementioned experimental results, a pathway of $^1O_2$ oxidation photocatalytic pollutant degradation is proposed in Fig. 17a.

Detailed mechanisms for photocatalytic phenol and NO_x removal by pure TiO_2 have previously been reported (Turki et al. 2015; Dalton et al. 2002; Dang et al. 2016). For phenol degradation, the contaminant is first hydroxylated forming hydroquinone and/or catechol. Parallel formation of benzoquinone and carboxylic acids (e.g., propionic acid, formic acid, maleic acid…) has been previously observed (Turki et al. 2015; Dang et al. 2016). Intermediates could be further oxidized into to short-chain organic compounds, and due to the weak energy of C–H, H–O, and C–O bonds, these can be easily mineralized to carbon dioxide and water (Turki et al. 2015; Dang et al. 2016; Pankaj et al. 2017; Trinh et al. 2016). For the mechanism of NO_x removal is commonly assumed that NO is adsorbed onto the catalysts' surface and converts to HNO_2 and NO_2. The HNO_2 formed is totally consumed and converted into NO_2, as its reaction is very fast, while NO_2 either converts to HNO_3 or desorbs (Bloh et al. 2014; Dalton et al. 2002; Ângelo et al. 2013). As an initial approximation, our findings indicated that these

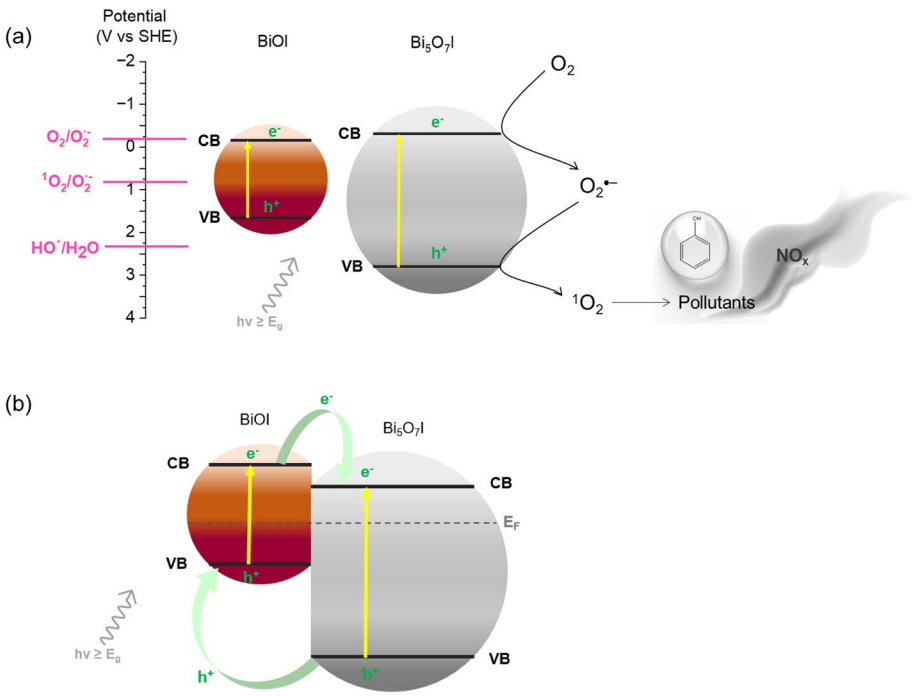

Fig. 17 **a** $^1O_2$ proposed photocatalytic mechanism of synthesized bismuth oxyiodides and **b** proposed charge transfer mechanism of BiOI/Bi_5O_7I-co pH 12

degradation pathways and their associated intermediates might be extrapolated to this work using bismuth oxyiodides materials, but further research is required.

Besides this, it is generally accepted that for pure TiO_2 system, HO· is the main oxidation specie responsible for NO_x (Rhimi et al. 2022) and phenol degradation (Chiou et al. 2008; Trillas et al. 1992). These pollutants can be oxidized by either photogenerated h^+ (Jimenez-Relinque and Castellote 2015) or other active species (HO· and $O_2{\cdot}^-$) (Nava-Núñez et al. 2020; Wysocka et al. 2018). Thus, up to date, the photocatalytic action of TiO_2 appeared to be the sum of these oxidative processes (Jimenez-Relinque et al. 2024). However, the ROS-photocatalytic oxidation mechanism of bismuth oxide remains unclear in literature and may differ from one to another. For example, recent research by Li et. al. (Li and Meng 2020) revealed that h^+ may be the main oxidant for phenol degradation in a range of bismuth-based photocatalytic systems (Bi_2WO_6, Bi_2MoO_6, BiOBr, BiOCl, BiOI, $BiPO_4$, and $Bi_2O_2CO_3$), where HO· and $O_2{\cdot}^-$ are produced insignificantly. In contrast, according to Wu et al. (Wu et al. 2017) BI_5O_7I phenol degradation is mainly mediated by $O_2{\cdot}^-$., and in the case of BiOI microspheres, Wang et al. (Wang et al. 2017b) report the involvement of both HO· and $O_2{\cdot}^-$. Discrepancies in results have also been observed in NO_x oxidation studies. Nava-Núñez et al. (Nava-Núñez et al. 2020) and Gangqiang Zhu et al. (Zhu et al. 2019) proposed no HO· generation in BiOI but instead reported the involvement of $O_2{\cdot}^-$. In contrast, Dong et al. (Dong et al. 2015) demonstrated even changes during the photocatalytic oxidation process of BiOI materials. They propose that initially the HO· governs the oxidation of NO, but the accumulation of NO_3^- on catalyst surface may inhibit their generation, changing the process to selective oxidation by h^+. Based on our analysis supported by different ROS-detection methods (quencher experiments, EPR, and TA-FL probe method), this study opens a new via of photocatalytic conversion processes of bismuth oxyiodides involving $^1O_2$ and absence of HO· participation. Hence, a comprehensive grasp of the ROS photocatalytic degradation pathways is still essential for understanding the photocatalytic efficacy in the range of bismuth oxyiodide systems. Thus, in-depth mechanistic studies to understand the underlying processes involved would be very interesting to propose comprehensive mechanisms. These lines of inquiry can open new perspectives for designing and optimizing efficient photocatalysts in environmental pollutant degradation.

Moreover, for BiOI/Bi_5O_7I-co pH 12, a charge transfer mechanism has been proposed in Fig. 17b. After heterojunction formation, electrons transfer from the CB of BiOI to the CB of Bi_5O_7I, and holes transfer from the VB of Bi_5O_7I to the VB of BiOI, which make the Fermi level of BiOI/Bi_5O_7I-co pH 12 reach a new equilibrium state. The E_F of BiOI/Bi_5O_7I-co pH 12 has been estimated to be − 0.23 V vs SHE, through Mott Schottky plot (Fig. S7) and unit conversion using Eq. 1. Given that it is closer to the Fermi level estimated for the Bi_5O_7I sample alone (-co pH 13; $E_F = -0.28$ V vs SHE), it can be concluded that the most likely mechanism is the transfer of electrons to this phase. This is in accordance with mechanisms proposed previously in the literature for BiOI/Bi_5O_7I (Liao et al. 2021; Yu et al. 2024).

Conclusions

Bismuth oxyiodides (BiOI, BiOI/Bi_5O_7I, and Bi_5O_7I) were effectively synthesized through co-precipitation and hydrothermal procedures. Photocatalytic activity was evaluated for phenol decomposition in water solution and NO_x air purification. While TiO_2 under UV light substantially enhanced removal efficiency in both tests, BiOI-co pH 10 and BiOI/Bi_5O_7I-co pH 12 demonstrated promising efficiencies under visible light. The enhanced efficiency of this is a combination of suitable optical properties (E_g and e^--h^+ recombination) and microstructure parameters (higher S_{BET}). However, photocatalytic activities for bismuth oxyiodides under visible light were lower than TiO_2 under UV light. This suggests that in order to hasten the practical application and commercialization of these innovative materials, strategies for improving the photocatalytic activity of bismuth oxyiodides under visible/solar light are necessary.

Bi_5O_7I-UV, BiOI/Bi_5O_7I-VIS, and TiO_2 P25-UV systems displayed equivalent mineralization capabilities in terms of TOC/phenol ratios. Bismuth-based oxyiodides only produce traces of hydroquinone intermediate during the phenol conversion process but produced more intermediate NO_2 during NO oxidation than the benchmark TiO_2 P25. This suggest that phenol degradation by-products might adsorb onto the bismuth oxyiodides surface. However, a different mediated mechanism cannot be neglected. Various ROS detection methods revealed that HO· is not the major oxidant specie in the photocatalytic degradation of bismuth oxyiodides, even in the case of Bi_5O_7I, where the formation of HO· was thermodynamically favored due to the position of its valence band. An alternative pathway is suggested, focusing on $^1O_2$, a less oxidative ROS. This might partially explain the lower photocatalytic efficiencies and selectivity of Bi_5O_7I. However, the influence of the structural properties (rod-like morphology and low S_{BET}) as limiting factor cannot be neglected.

Supplementary Information

The online version contains supplementary material available at https://doi.org/10.1186/s40712-025-00251-6.

Supplementary Material 1. Supplementary figures: Figure S1. DRX spectra of repeated synthesis. Figure S2. Emission spectra of the irradiance sources. Figure S3. EDX results of samples synthesized via pH-dependent co-precipitation and hydrothermal procedures. Ten points were taken for SEM-EDX analyses to calculate Bi:O:I ratios. The spectra of point 9 are provide as an example. Figure S4. FTIR spectra of samples synthesized via pH-dependent co-precipitation and hydrothermal procedures. TiO_2 P25 is also included. Figure S5. Nitrogen adsorption/desorption isotherms and the corresponding pore size distributions. Figure S6. X band continuous wave EPR experimental spectraand simulations of DMPOX and DMPO-OH. Figure S7. Mott-Shottky plot of BiOI/Bi_5O_7I-co pH 12.

Acknowledgements
The authors would like to thank the scientific and technical services of the Eduardo Torroja Institute of Construction Sciences (IETcc-CSIC) and the Nuclear Magnetic Resonance Service of the Biological Research Center (CIB-CSIC).

Authors' contributions
AM-T, writing — original draft, visualization, methodology, investigation, data curation, and conceptualization. EJ-R, writing — review and editing, validation, supervision, methodology, investigation, and funding acquisition. FD, writing — review and editing, validation, methodology, and investigation. SS, writing — review and editing, validation, methodology, and investigation. AG, writing — review and editing, validation, methodology, and investigation. TS, writing — review and editing, validation, methodology, and investigation. CG, writing – review and editing, validation, supervision, methodology, and investigation. AF, writing — review and editing, validation, supervision, methodology, and investigation. MC, writing — review and editing, validation, supervision, methodology, investigation, and funding acquisition.

Funding
The funding for this work was provided by the projects PID2022-141812OB-I00 from the AIE (Spanish Research Agency) and ILINK22054 from CSIC. We would also want to thank the Ministry of Universities (Spain) for its financial support through the FPU22/01793 predoctoral scholarship to Andrea Martínez-Topete.

Data availability
Not applicable.

Declarations

Competing interests
The authors declare that they have no competing interests.

Author details
[1]Institute of Construction Science Eduardo Torroja (IETcc-CSIC), Madrid, Spain. [2]Escuela Técnica Superior de Ingenieros Industriales, Universidad Politécnica de Madrid (UPM), Madrid, Spain. [3]Institut de Recherches Sur La Catalyse Et L'Environnement de Lyon (IRCELYON), UMR5256, Université Claude Bernard Lyon 1, CNRS, Lyon, Villeurbanne 69626, France. [4]School of Chemistry, Cardiff University, Main Building, Park Place, Cardiff CF10 3AT, UK. [5]School of Chemistry, Cardiff Catalysis Institute, Cardiff University, Cardiff CF10 3AT, UK. [6]School of Chemistry, Translational Research Hub, Net Zero Innovation Institute, Cardiff Catalysis Institute, Cardiff University, Maindy Road, Cardiff CF24 4HF, UK.

Received: 10 October 2024 Accepted: 2 March 2025
Published online: 18 March 2025

References

Ahmad I, Shukrullah S, Naz MY, Ullah S, Assiri MA (2022) Designing and modification of bismuth oxyhalides BiOX (X= Cl, Br and I) photocatalysts for improved photocatalytic performance. J Ind Eng Chem 105:1–33

Alcaraz L, Jiménez-Relinque E, Plaza L, García-Díaz I, Castellote M, López FA (2020) Photocatalytic activity of $Zn_xMn_{3-x}O_4$ Oxides and ZnO prepared from spent alkaline batteries. Front Chem 8:552380

Al-Nu'airat J, Dlugogorski BZ, Gao X, Zeinali N, Skut J, Westmoreland PR, Oluwoye I, Altarawneh M (2019) Reaction of phenol with singlet oxygen. Phys Chem Chem Phys 21(1):171–183

Ângelo J, Andrade L, Madeira LM, Mendes A (2013) An overview of photocatalysis phenomena applied to NOx abatement. J Environ Manage 129:522–539

Arumugam M, Choi MY (2020) Recent progress on bismuth oxyiodide (BiOI) photocatalyst for environmental remediation. J Ind Eng Chem 81:237–268

Bairamis F, Konstantinou I (2021) WO_3 fibers/g-C_3N_4 Z-scheme heterostructure photocatalysts for simultaneous oxidation/reduction of phenol/Cr (VI) in aquatic media. Catalysts 11(7):792

Balázs N, Gácsi A, Pallagi A, Mogyorósi K, Alapi T, Sipos P, Dombi A (2011) Comparison of the liquid and gas phase photocatalytic activity of flame-synthesized TiO_2 catalysts: the role of surface quality. React Kinet Mech Catal 102(2):283–294

Bloh JZ, Folli A, Macphee DE (2014) Photocatalytic NO x abatement: why the selectivity matters. RSC Adv 4(86):45726–45734

Cai L, Yao J, Li J, Zhang Y, Wei Y (2019) Sonochemical synthesis of BiOI-TiO_2 heterojunction with enhanced visible-light-driven photocatalytic activity. J Alloy Compd 783:300–309

Cao J, Li X, Lin H, Xu B, Luo B, Chen S (2012) Low temperature synthesis of novel rodlike Bi_5O_7I with visible light photocatalytic performance. Mater Lett 76:181–183

Chen R, Chen Z, Ji M, Chen H, Liu Y, Xia J, Li H (2018) Enhanced reactive oxygen species activation for building carbon quantum dots modified Bi_5O_7I nanorod composites and optimized visible-light-response photocatalytic performance. J Colloid Interface Sci 532:727–737

Chiou C-H, Wu C-Y, Juang R-S (2008) Influence of operating parameters on photocatalytic degradation of phenol in UV/TiO_2 process. Chem Eng J 139(2):322–329

Dai W-W, Zhao Z-Y (2016) Electronic structure and optical properties of BiOI as a photocatalyst driven by visible light. Catalysts 6(9):133

Dalton JS, Janes PA, Jones NG, Nicholson JA, Hallam KR, Allen GC (2002) Photocatalytic oxidation of NOx gases using TiO_2: a surface spectroscopic approach. Environ Pollut 120(2):415–422

Dang TTT, Le STT, Channei D, Khanitchaidecha W, Nakaruk A (2016) Photodegradation mechanisms of phenol in the photocatalytic process. Res Chem Intermed 42(6):5961–5974

Di J, Xia J, Li H, Guo S, Dai S (2017) Bismuth oxyhalide layered materials for energy and environmental applications. Nano Energy 41:172–192

Dong G, Ho W, Zhang L (2015) Photocatalytic NO removal on BiOI surface: the change from nonselective oxidation to selective oxidation. Appl Catal B 168–169:490–496

Finkelstein E, Rosen GM, Rauckman EJ (1982) Production of hydroxyl radical by decomposition of superoxide spin-trapped adducts. Mol Pharmacol 21(2):262–265

Folli A, Bloh JZ, Strøm M, Pilegaard Madsen T, Henriksen T, Macphee DE (2014) Efficiency of solar-light-driven TiO_2 photocatalysis at different latitudes and seasons. Where and when does TiO2 really work? 5(5):830–832

Fujishima A, Rao TN, Tryk DA (2000) Titanium dioxide photocatalysis. J Photochem Photobiol, C 1(1):1–21

Gao X, Zhang X, Wang Y, Peng S, Yue B, Fan C (2015) Rapid synthesis of hierarchical BiOCl microspheres for efficient photocatalytic degradation of carbamazepine under simulated solar irradiation. Chem Eng J 263:419–426

Gao X, Gao K, Fu F, Liang C, Li Q, Liu J, Gao L, Zhu Y (2020) Synergistic introducing of oxygen vacancies and hybrid of organic semiconductor: realizing deep structure modulation on Bi_5O_7I for high-efficiency photocatalytic pollutant oxidation. Appl Catal B 265:118562

Ge F, Li X, Wu M, Ding H, Li X (2022) A type II heterojunction α-Fe 2 O 3/gC 3 N 4 for the heterogeneous photo-Fenton degradation of phenol. RSC Adv 12(14):8300–8309

Geng Q, Xie H, Ji W, Li Y, Chen S, Deng B, Jin R, Dong F (2024) Bismuth MOF-derived BiOI/Bi_5O_7I p-n heterojunctions with enhanced charge separation and visible-light photocatalytic performance. J Phys Chem 128(20):8331–8340

Guillard C, Disdier J, Herrmann J-M, Lehaut C, Chopin T, Malato S, Blanco J (1999) Comparison of various titania samples of industrial origin in the solar photocatalytic detoxification of water containing 4-chlorophenol. Catal Today 54(2):217–228

Hao R, Xiao X, Zuo X, Nan J, Zhang W (2012) Efficient adsorption and visible-light photocatalytic degradation of tetracycline hydrochloride using mesoporous BiOI microspheres. J Hazard Mater 209:137–145

Hassan QU, Channa AI, Zhai Q-G, Zhu G, Gao Y, Ali N, Bilal M (2022) Recent advancement in Bi_5O_7I-based nanocomposites for high performance photocatalysts. Chemosphere 288:132668

Herrmann J-M, Guillard C, Pichat P (1993) Heterogeneous photocatalysis: an emerging technology for water treatment. Catalysis Today 17(1–2):7–20

Hirakawa K, Oikawa S, Hiraku Y, Hirosawa I, Kawanishi S (2002) Catechol and hydroquinone have different redox properties responsible for their differential DNA-damaging ability. Chem Res Toxicol 15(1):76–82

Hu J, Weng S, Zheng Z, Pei Z, Huang M, Liu P (2014) Solvents mediated-synthesis of BiOI photocatalysts with tunable morphologies and their visible-light driven photocatalytic performances in removing of arsenic from water. J Hazard Mater 264:293–302

Huang J, Zhong S, Dai Y, Liu C-C, Zhang H (2018) Effect of MnO_2 phase structure on the oxidative reactivity toward bisphenol A degradation. Environ Sci Technol 52(19):11309–11318

Huang M, Peng S, Xiang W, Wang C, Wu X, Mao J, Zhou T (2022) Strong metal-support interaction between carbon nanotubes and Mn-Fe spinel oxide in boosting peroxymonosulfate activation: underneath mechanisms and application. Chem Eng J 429:132372

Ishibashi K-I, Fujishima A, Watanabe T, Hashimoto K (2000) Quantum yields of active oxidative species formed on TiO2 photocatalyst. J Photochem Photobiol, A 134(1):139–142

Jian Z, Hejing W (2003) The physical meanings of 5 basic parameters for an X-ray diffraction peak and their application. Chin J Geochem 22:38–44

Jimenez-Relinque E, Castellote M (2015) Quantification of hydroxyl radicals on cementitious materials by fluorescence spectrophotometry as a method to assess the photocatalytic activity. Cem Concr Res 74:108–115

Jimenez-Relinque E, Castellote M (2018) Hydroxyl radical and free and shallowly trapped electron generation and electron/hole recombination rates in TiO_2 photocatalysis using different combinations of anatase and rutile. Appl Catal A 565:20–25

Jimenez-Relinque E, Llorente I, Castellote M (2017) TiO_2cement-based materials: understanding optical properties and electronic band structure of complex matrices. Catal Today 287:203–209

Jimenez-Relinque E, Grande M, Duran T, Castillo Á, Castellote M (2020) Environmental impact of nano-functionalized construction materials: leaching of titanium and nitrates from photocatalytic pavements under outdoor conditions. Sci Total Environ 744:140817

Jimenez-Relinque E, Dappozze F, Berhault G, Gilbert C, Leonard D, Guillard C (2024) Bismuth oxyhalide as efficient photocatalyst for water, air treatment and bacteria inactivation under UV and visible light. J Photochem Photobiol, A 452:115554

Jin X, Ye L, Xie H, Chen G (2017) Bismuth-rich bismuth oxyhalides for environmental and energy photocatalysis. Coord Chem Rev 349:84–101

Kaleem Ahmad HRG, Ahuja SM (2020) A review on photocatalytic remediation of environmental pollutants and H_2 production through water splitting: a sustainable approach. Environ Technol Innov 9:100893

Kim H-H, Lee H, Lee D, Ko Y-J, Woo H, Lee J, Lee C, Pham AL-T (2020) Activation of hydrogen peroxide by a titanium oxide-supported iron catalyst: evidence for surface Fe (IV) and its selectivity. Environ Sci Technol 54(23):15424–15432

Koppenol WH, Stanbury DM, Bounds PL (2010) Electrode potentials of partially reduced oxygen species, from dioxygen to water. Free Radical Biol Med 49(3):317–322

Kynadi AS, Suchithra T (2017) Bacterial degradation of phenol to control environmental pollution, Microbial Biotechnology. Applications in Agriculture and Environment. 1:245–263

Lan M, Zheng N, Dong X, Hua C, Ma H, Zhang X (2020) Bismuth-rich bismuth oxyiodide microspheres with abundant oxygen vacancies as an efficient photocatalyst for nitrogen fixation. Dalton Trans 49(26):9123–9129

Lee WW, Lu C-S, Chuang C-W, Chen Y-J, Fu J-Y, Siao C-W, Chen C-C (2015) Synthesis of bismuth oxyiodides and their composites: characterization, photocatalytic activity, and degradation mechanisms. RSC Adv 5(30):23450–23463

Li Z, Meng X (2020) New insight into reactive oxidation species (ROS) for bismuth-based photocatalysis in phenol removal. J Hazard Mater 399:122939

Li J, Wu N (2015) Semiconductor-based photocatalysts and photoelectrochemical cells for solar fuel generation: a review. Catal Sci Technol 5(3):1360–1384

Liao H, Li Z, Luo L, Zhong J, Li J (2021) Water hyacinth powder -assisted preparation of defects-rich and flower-like $BiOI/Bi_5O_7I$ heterojunctions with excellent visible light photocatalytic activity. Surfaces and Interfaces 27:101470

Lin J, Hu Z, Li H, Qu J, Zhang M, Liang W, Hu S (2019) Ultrathin nanotubes of Bi_5O_7I with a reduced band gap as a high-performance photocatalyst. Inorg Chem 58(15):9833–9843

Liu C, Wang X-J (2016) Room temperature synthesis of $Bi_4O_5I_2$ and Bi_5O_7I ultrathin nanosheets with a high visible light photocatalytic performance. Dalton Trans 45(18):7720–7727

Liu QY, Zheng YF, Wang L, Song XC (2019) Synthesis of $BiIO_4/Ag_3PO_4$nanocomposite with enhanced photocatalytic activity for degradation of phenol. J Nanopart Res 21:1–9

Liu Q-H, Wang H-L, Huang H, Jiang W-F (2023) Erythritol assisted facile green synthesis of bismuth-rich photocatalyst $Bi_7O_9I_3$ with enhanced photocatalytic degradation performance. J Environ Chem Eng 11(5):110611

Long Y, Wang Y, Zhang D, Ju P, Sun Y (2016) Facile synthesis of BiOI in hierarchical nanostructure preparation and its photocatalytic application to organic dye removal and biocidal effect of bacteria. J Colloid Interface Sci 481:47–56

López Zavala MÁ, Lozano Morales SA, Ávila-Santos M (2017) Synthesis of stable TiO_2 nanotubes: effect of hydrothermal treatment, acid washing and annealing temperature. Heliyon 3(11):e00456

Lu Y, Sun Y, Li J, Xu Y, Han Q, Wei L, Sun J, Guo J (2022) Preparation of a novel pn $BiOI/Bi_2WO_6$photocatalyst and its application in the treatment of tetracycline. J Mater Sci: Mater Electron 33(29):23212–23223

Ma R, Zhang S, Liu X, Sun M, Cao J, Wang J, Wang S, Wen T, Wang X (2022) Oxygen defects-induced charge transfer in $Bi_7O_9I_3$for enhancing oxygen activation and visible-light degradation of BPA. Chemosphere 286:131783

Makuła P, Pacia M, Macyk W (2018) How to correctly determine the band gap energy of modified semiconductor photocatalysts based on UV–Vis spectra. The Journal of Physical Chemistry Letters 9(23):6814–6817

Malato S, Blanco J, Vidal A, Richter C (2002) Photocatalysis with solar energy at a pilot-plant scale: an overview. Appl Catal B: Environ 37(1):1–15

Martinez-Topete A, Robles M, Perez G, Martin-Consuegra F, Castellote M, Jimenez-Relinque E (2025) Ecofriendly multifunctional bismuth oxyiodides pigment and paint coatings: Photocatalytic and cooling functionalities. J Photochem Photobiol, A 460:116151

Matiur RM, Abuelwafa A, Kato S, Kishi N, Soga T (2021) A comparative study on optical properties of BiOI, $Bi_7O_9I_3$ and Bi_5O_7I materials. Opt Mater 111:110677

Mera AC, Rodríguez C, Meléndrez M, Valdés H (2017) Synthesis and characterization of BiOI microspheres under standardized conditions. J Mater Sci 52:944–954

Michael STM, Hoffmann R, Choi W, Bahnemann DW (1995) Environmental applications of semiconductor photocatalysis. Chem Rev 95(1):69–96

Nava-Núñez MY, Jimenez-Relinque E, Grande M, Martínez-de la Cruz A, Castellote M (2020) Photocatalytic BiOX mortars under visible light irradiation: compatibility, NOx efficiency and nitrate selectivity. Catalysts 10(2):226

Nevshupa R, Jimenez-Relinque E, Grande M, Martinez E, Castellote M (2020) Assessment of urban air pollution related to potential nanoparticle emission from photocatalytic pavements. J Environ Manage 272:111059

Ngo T-H, Le P-N-M, Truong C-H, Huynh N-D-T, Tran T-H, Luan V-H, Dang B-T, Rafie Johan M, Sagadevan S, Le M-V (2024) Development of bismuth-rich bismuth oxyhalides based photocatalyst for degradation of a representative antibiotic under simulated solar light irradiation. Journal of Photochemistry and Photobiology A: Chemistry 446:115157

Nosaka Y, Nosaka AY (2017) Generation and detection of reactive oxygen species in photocatalysis. Chem Rev 117(17):11302–11336

Nosaka Y, Komori S, Yawata K, Hirakawa T, Nosaka AY (2003) Photocatalytic OH radical formation in TiO 2 aqueous suspension studied by several detection methods. Phys Chem Chem Phys 5(20):4731–4735

Pallotti DK, Passoni L, Maddalena P, Di Fonzo F, Lettieri S (2017) Photoluminescence mechanisms in anatase and rutile TiO2. The Journal of Physical Chemistry C 121(16):9011–9021
Pankaj C, Sharmistha N, Ajay KR (2017) Degradation of phenolic compounds through UV and visible- light-driven photocatalysis: technical and economic aspects, in: S.H. Marcos, P.T. Mariana, G.M. Maria del Rosario (Eds.), Phenolic compounds, IntechOpen, Rijeka. p. Ch. 16
Reyna-Cavazos KA, la Cruz AMD, Longoria Rodríguez FE, López-Cuellar E (2020) Synthesis of bismuth oxyiodide (BiOI) by means of microwaves in glycerol with high photocatalytic activity for the elimination of NOx and SO_2. Res Chem Intermed 46(1):923–941
Rhimi B, Padervand M, Jouini H, Ghasemi S, Bahnemann DW, Wang C (2022) Recent progress in NOx photocatalytic removal: surface/interface engineering and mechanistic understanding. J Environ Chem Eng 10(6):108566
Schneider J, Matsuoka M, Takeuchi M, Zhang J, Horiuchi Y, Anpo M, Bahnemann DW (2014) understanding TiO_2 photocatalysis: mechanisms and materials. Chem Rev 114(19):9919–9986
Shi X, Chen X, Chen X, Zhou S, Lou S (2012) Solvothermal synthesis of BiOI hierarchical spheres with homogeneous sizes and their high photocatalytic performance. Mater Lett 68:296–299
Skocaj M, Filipic M, Petkovic J, Novak S (2011) Titanium dioxide in our everyday life; is it safe? Radiol Oncol 45(4):227
Trillas M, Pujol M, Domènech X (1992) Phenol photodegradation over titanium dioxide. J Chem Technol Biotechnol 55(1):85–90
Trinh D, Le S, Channei D, Khanitchaidecha W, Nakaruk A (2016) Investigation of intermediate compounds of phenol in photocatalysis process. Int J Chem Eng Appl 7(4):273–276
Tuba-Guaman D, Zuarez-Chamba M, Quishpe-Quishpe L, Reinoso C, Santacruz CP, Herrera-Robledo M, Cisneros-Pérez PA (2022) Photodegradation of rhodamine B and bisphenol A over visible-light driven Bi7O9I3-and Bi12O17Cl2-photocatalysts under white LED irradiation. Top Catal 65(9–12):1028–1044
Turki A, Guillard C, Dappozze F, Ksibi Z, Berhault G, Kochkar H (2015) Phenol photocatalytic degradation over anisotropic TiO_2 nanomaterials: kinetic study, adsorption isotherms and formal mechanisms. Appl Catal B 163:404–414
Wang G, Xu L, Zhang J, Yin T, Han D (2012) Enhanced photocatalytic activity of powders (P25) via calcination treatment. Int J Photoenergy 2012:265760
Wang W, Huang Y, Zhang X, Cao J-J, Ho W, Lee SC (2017) Three-dimensional Bi_5O_7I photocatalysts for efficient removal of NO in air under visible light. Aerosol Science and Engineering 1(1):33–40
Wang X, Song Y, Hou J, Chen X (2017) Fabrication of BiOI hierarchical microspheres with efficient photocatalysis for methylene blue and phenol removal. Cryst Res Technol 52(7):1700068
Wang H, Li K, Li J, Sun Y, Dong F (2021) Photochemical transformation pathways of nitrates from photocatalytic NOx oxidation: implications for controlling secondary pollutants. Environ Sci Technol Lett 8(10):873–877
Wei Y, Su H, Zhang Y, Zheng L, Pan Y, Su C, Geng W, Long M (2019) efficient peroxodisulfate activation by iodine vacancy rich bismuth oxyiodide: a vacancy induced mechanism. Chem Eng J 375:121971
Wu G, Zhao Y, Li Y, Zhang F, Zhao J (2017) Assembled and isolated Bi_5O_7I nanowires with good photocatalytic activities. CrystEngComm 19(15):2113–2125
Wu G, Zhao Y, Li Y, Ma H, Zhao J (2018) pH-dependent synthesis of iodine-deficient bismuth oxyiodide microstructures: visible-light photocatalytic activity. J Colloid Interface Sci 510:228–236
Wysocka I, Kowalska E, Trzciński K, Łapiński M, Nowaczyk G, Zielińska-Jurek A (2018) UV-Vis-induced degradation of phenol over magnetic photocatalysts modified with Pt, Pd, Cu and Au nanoparticles. Nanomaterials (Basel) 8(1):28
Xia Y, He Z, Su J, Tang B, Liu Y (2018) Enhanced photocatalytic performance of Z-scheme Cu_2O/Bi_5O_7I nanocomposites. J Mater Sci: Mater Electron 29(17):15271–15281
Xiao X, Zhang W-D (2010) Facile synthesis of nanostructured BiOI microspheres with high visible light-induced photocatalytic activity. J Mater Chem 20(28):5866–5870
Xiao X, Hao R, Zuo X, Nan J, Li L, Zhang W (2012) Microwave-assisted synthesis of hierarchical $Bi_7O_9I_3$ microsheets for efficient photocatalytic degradation of bisphenol-A under visible light irradiation. Chem Eng J 209:293–300
Xiao X, Xing C, He G, Zuo X, Nan J, Wang L (2014) Solvothermal synthesis of novel hierarchical $Bi_4O_5I_2$ nanoflakes with highly visible light photocatalytic performance for the degradation of 4-tert-butylphenol. Appl Catal B 148:154–163
Xiong J, Song P, Di J, Li H (2020) Bismuth-rich bismuth oxyhalides: a new opportunity to trigger high-efficiency photocatalysis. Journal of Materials Chemistry A 8(41):21434–21454
Yang CZY, Lai C, Zeng G, Huang D, Cheng M, Wang J, Chen F, Zhou C, Xiong W (2018) BiOX (X = Cl, Br, I) photocatalytic nanomaterials: applications for fuels and environmental management. Adv Colloid Interface Sci 254:76–93
Ye L, Jin X, Ji X, Liu C, Su Y, Xie H, Liu C (2016) Facet-dependent photocatalytic reduction of CO_2 on BiOI nanosheets. Chem Eng J 291:39–46
Yu Y, Chen G, Wang X, Jia D, Tang P, Lv C (2015) A facile approach to construct $BiOI/Bi_5O_7I$ composites with heterostructures: efficient charge separation and enhanced photocatalytic activity. RSC Adv 5(91):74174–74179
Yu H, He Z, Zhang Y, Ng LS, Ni J, Guo F, Hu J, Lee HK, Han J (2024) In situ reversible assembly of atomic interfacial structure in $BiOI/Bi_5O_7I$ p-n heterojunctions to promote visible-light photocatalysis. Chem Eng J 481:148350
Zhang L, Zhai T, Yang M, Hu C (2022) Few-layered $Bi_4O_5I_2$ nanosheets enclosed by 1 0–1 facets with oxygen vacancies for highly-efficient removal of water contaminants. J Hazard Mater 437:129274
Zhao J, Yang X (2003) Photocatalytic oxidation for indoor air purification: a literature review. Building Environment 38:645–654
Zhu G, Hojamberdiev M, Zhang S, Din STU, Yang W (2019) Enhancing visible-light-induced photocatalytic activity of BiOI microspheres for NO removal by synchronous coupling with Bi metal and graphene. Appl Surf Sci 467–468:968–978
Zhu L, Ji J, Liu J, Mine S, Matsuoka M, Zhang J, Xing M (2020) Designing 3D-MoS_2 sponge as excellent cocatalysts in advanced oxidation processes for pollutant control. Angew Chem 132(33):14072–14080
Zuarez-Chamba M, Tuba-Guamán D, Quishpe M, Pazmiño K, Vizuete K, Debut A, Cisneros-Pérez PA, Reinoso C, Santacruz C, Salgado A (2023) Synthesis of $Bi_4O_5I_2$ microbars for pollutant degradation through a photocatalytic process. Mater Lett 336:133888

Publisher's Note